Tidal Distortion and Disruption of Earth-Crossing Asteroids

Derek C. Richardson[†]
Department of Astronomy
University of Washington
Box 351580
Seattle, WA 98195-1580
Tel: (206) 543-0206
Fax: (206) 685-0403
dcr@astro.washington.edu

William F. Bottke, Jr.
Center for Radiophysics & Space Research
306 Space Sciences
Cornell University
Ithaca, NY 14853-6801
Tel: (607) 255-3934
Fax: (607) 255-9002
bottke@astrosun.tn.cornell.edu

Stanley G. Love[‡]
Seismological Laboratory
California Institute of Technology
Mail Code 252-21
Pasadena, CA 91125

Prepared for *Icarus*
[illegible] 2, 1997

00 manuscript pages
0 figures
0 tables
Running page head: Tidal Disruption of Asteroids

[†] To whom correspondence should be addressed

[‡] Now at Jet Propulsion Laboratory, Mail Stop 306-438, 4800 Oak Grove Drive, Pasadena, CA 91109, Tel: (818) 354-9084, Fax: (818) 393-4773, Stanley.G.Love@jpl.nasa.gov.

Abstract

We present results of numerical simulations that show Earth's tidal forces can both distort and disrupt Earth-crossing asteroids (ECAs) that have weak "rubble-pile" [illegible]. Building on previous studies, we consider more realistic asteroid shapes and trajectories, test a variety of spin rates and axis orientations, and employ a dissipation algorithm to more accurately treat collisions between particles. We explore a large parameter space, including the asteroid's periapse q, encounter velocity with the Earth v_∞, spin period P (including a no-spin case), spin axis orientation, and body orientation at periapse.

We identify four outcome classes parameterized by the amount of mass stripped from the asteroid during a flyby. Our most severe disruptions result in fragment trains similar in character to the "string of pearls" created when comet Shoemaker-Levy-9 was disrupted near Jupiter in 1992. Less catastrophic disruptions cause material to be stripped off in more isotropic fashion, leaving a central remnant with a characteristic distorted shape. Some ejecta can enter into stable orbits around the remnant, creating a binary or multiple system. Even when no mass is lost, we still find that tidal forces can modify the asteroid's shape and spin.

Our results show that mass loss is enhanced for small values of q, v_∞, and P, and depends to a certain extent on the body's spin orientation (for example, retrograde rotation reduces mass loss). An elongated asteroid was found to be far easier to disrupt than a spherical one, though the orientation of the ellipsoid at periapse can noticeably change the outcome. The size and orbital distribution of the ejecta are discussed, along with many of the applications of this technique toward an understanding of unusual phenomena in the terrestrial region (e.g., origin of certain crater chains on the Moon, doublet craters on the terrestrial planets, irregular shaped ECAs, etc.).

Keywords: Tides, Solid Body; Asteroids, General; Planetesimals; Cratering, Terrestrial; Computer Techniques [other possibilities: Asteroids, Composition; Asteroids, Dynamics; Asteroids, Rotation; Celestial Mechanics; Collisional Physics; Impact Processes, Asteroids; Orbits, Asteroids; Planetary Dynamics; Radar, Asteroids; MORE???]

1 INTRODUCTION

1.1 Evidence for "Rubble-pile" Asteroids

There is an increasing body of evidence to suggest that Earth-crossing asteroids (ECAs) are "rubble-piles", self-gravitating collections of smaller fragments that may be susceptible to tidal distortion and disruption.

Chapman (1978) was one of the first to seriously propose that high velocity collisions between asteroids in the main-belt could fracture and erode these monolithic bodies into "piles of boulders" (see also Davis and Chapman 1977). This scenario was given new credibility when 243 Mathilde, a ~ 53 km C-type main-belt asteroid, was imaged by the Near-Earth Asteroid Rendezvous (NEAR) spacecraft in June 1997. Several surprisingly large craters between 20 and 30 km in diameter were seen on Mathilde's illuminated surface (Yeomans 1997). Numerical hydrocode models of asteroid collisions suggest craters this large could only have formed in the "gravity-scaling" regime, where the growth and ultimate size of a crater is controlled by the target's gravity rather than its physical strength (Greenberg *et al.* 1994; 1996; Asphaug *et al.* 1996a; Love and Ahrens 1996). Craters formed in the gravity regime require a weak or fragmented target much like a rubble-pile. If any of these craters had formed in the "strength" regime, they would have instead disrupted the target. Supporting this view is Mathilde's estimated density, ~ 1.3 g cm^{-3}, or roughly half that of carbonaceous chondrites (Wasson 1974). If C-class asteroids are indeed the parent bodies of this meteorite class (Wasson 1974), then the interior of Mathilde must either contain large void spaces or consist of small packed fragments with substantial interparticle porosity. Either structure is inconsistent with the conventional picture of an asteroid being solid rock left intact after billions of years of impacts.

Numerical hydrocode models reveal how rubble-piles may be formed. When a moderate-sized body strikes a solid target, the crater excavation is preceded by an advancing shock front which shatters the material as it passes through. Thus, even a single impact can change an initially undamaged asteroid into a highly fractured one consisting of large blocks of material. Subsequent collisions will continue to do damage, though the discontinuous inner structure of the target will make it difficult for the shock front to propagate beyond the boundaries of individual boulders near the impact site (Asphaug *et al.* 1996b). Rubble-piles, therefore, are even harder to disrupt or pulverize than solid objects.

Images of large craters on 243 Ida, 951 Gaspra, and Phobos lend credence to this theory: Ida, with dimensions of $60 \times 26 \times 18$ km, has one ~ 23 km crater and five ~ 10 km craters (Belton *et al.* 1994; Thomas *et al.* 1996); Gaspra, with dimensions of $18 \times 11 \times 9$ km, could have as many as eight craters larger than 4 km in diameter (Belton *et al.* 1992; Greenberg *et al.* 1994); Phobos (dimensions $27 \times 22 \times 19$ km) is dominated by the large crater Stickney (11 km) (Asphaug and Melosh 1993). Numerical hydrocode simulations of these crater forming events indicate the target, in each case, is left with a highly damaged and fragmented structure (Asphaug and Melosh 1993; Greenberg *et al.* 1994; 1996).

Since most Earth-crossing asteroids are thought to be fragments of shattered main-belt asteroids which have been delivered to the terrestrial planet region by the 3:1 and ν_6 chaotic resonances (Wisdom 1983; Morbidelli and Moons 1995; Gladman *et al.* 1997), we claim that most (if not all) ECAs larger than a few hundred meters in diameter are rubble-piles (Love and Ahrens 1996).

This view is supported by the spin period distribution of asteroids, compiled by Harris (1996). Harris derived the critical density ρ_c below which the centrifugal acceleration of a elongated body rotating with spin period P exceeds its gravitational acceleration, at which point it begins to shed mass along its equator:

$$\rho_c \sim \left(\frac{3.3\ \mathrm{h}}{P}\right)^2 \left(\frac{a}{b}\right) \mathrm{g\ cm^{-3}} \sim \left(\frac{3.3\ \mathrm{h}}{P}\right)^2 (1 + \Delta m)\ \mathrm{g\ cm^{-3}}, \tag{1}$$

where the axis ratio of the rubble-pile projected on the sky is a/b and the lightcurve amplitude of the body has magnitude Δm. Plotting lightcurve amplitudes *vs.* spin period for 688 asteroids of all sizes, Harris found that no asteroid spins faster than the disruption limit for a density of $\rho_c \sim 2.7$ g cm^{-3}. He then examined the spin period distribution of the 107 asteroids smaller than 10 km diameter in his sample, many of which are ECAs. Harris found this distribution abruptly truncates at fast spin rates. Since asteroids with tensile strength can rotate at virtually any speed, this truncation implies that ECAs may have no tensile strength and therefore may be rubble-piles.

There is considerable evidence that some comets may also be rubble-piles. Indirect observational and theoretical considerations (e.g., spontaneous nucleus splitting, Weissman 1982; formation through accretion of smaller icy components, Weidenschilling 1997; *etc.*) and the more direct record of tidally disrupted comets, together strongly imply that comets are intrinsically weak objects.

The most famous disrupted comet is without question Shoemaker-Levy-9 (SL9), which broke into more than 20 similar sized fragments during its penultimate encounter with Jupiter in 1992, when it passed within

1.6 Jovian radii of the planet center. Asphaug and Benz (1996) found that SL 9's disruption into a "string of pearls" could only have occurred if the comet was virtually strengthless (*cf.* Section 1.2). Another tidally disrupted comet (of less renown) is P/Brooks 2, which broke into at least 8 fragments when it approached within 2 Jovian radii of Jupiter in 1886 (Sekanina and Yeomans 1985). However, *not all objects break apart* on close approach. comet P/Gehrels 3 remained intact after approaching within 3 Jovian radii of Jupiter (Rickman 1979; Rickman and Malmort 1981), though this result was *consistent* with the tidal disruption limit predicted by Sridhar and Tremaine (1992) (*cf.* Eq. (3), below).

At least three sun-grazing comets are believed to have been pulled apart by solar tides rather than disrupted by volatile pressure over the last ~100 yr: P/Great September Comet (1882), P/Pereyra (1963), and P/Ikeya-Seki (1965) (Weissman 1980). In the case of [illegible], Öpik (1966) argued that the seven identifiable fragments, all of which had perihelia near 0.008 AU but diverse aphelia separated by as much as 6 AU, required a dynamic separation mechanism like tidal disruption. Typical comet splitting mechanisms (e.g., pressure release from volatile gas pockets, explosive radicals, amorphous ice, jetting of volatiles) only produce velocities of a few m s^{-1}. Öpik also determined that if the comet did not have a rubble-pile structure, it would have to be weaker than "meteoric dustballs" to disrupt.

The fragmentation of these comets vividly demonstrates how even weak differential gravity can drastically alter the morphology of small bodies in the solar system. The frequency of SL9 events near Jupiter is not known, but the cratering records of the Galilean satellites suggest that SL9 was not a singular occurrence. Unusual crater chains called catenae, classified as having long, linear rows of equally spaced, similarly sized craters, have been identified on the Jupiter-facing hemispheres of Ganymede and Callisto (Schenk *et al.* 1996). Melosh and Schenk (1993) have suggested that the catenae are impact scars from SL9-like fragment trains, especially since their morphology and location are inconsistent with secondary chains formed by crater ejecta. Since both Ganymede and Callisto are relatively small targets far from Jupiter, SL9-type events would need to occur every 200–400 years to produce the observed number of catenae on each body (Schenk *et al.* 1996). Thus we can infer that tidal disruption is common near Jupiter.

We hypothesize that tidal disruption may also occur near Earth. The Earth is smaller than Jupiter, but it is also more dense, enhancing the strength of tidal forces. It is also approached more often by slow-moving asteroids than by high-speed comets; the higher density of asteroids makes them harder to pull apart, but their lower speeds allow more time for tidal forces to work. Since we have yet to see an event comparable to SL9 near Earth, however, we must look elsewhere for evidence that tidal disruption does occur.

Three main lines of evidence have emerged which support our hypothesis. First, surveys of the lunar surface have revealed one or two catenae on the Moon's near side analogous to those seen on the Galilean satellites (Melosh and Whitaker 1994; Watchman and Wood 1995; Sterich et al 1996). These could have resulted from SL9-like disruption of ECAs (Bottke *et al.* 1997a). Second, doublet craters – impact structures that are thought to be formed by two asteroids striking a planetary surface at nearly the same time have been found on the Earth, Moon, Venus, and Mars (Melosh and Stansberry 1991). These exceptional features can be explained by the impact of well-separated binary asteroids produced by tidal disruption events near Earth (Bottke and Melosh 1996a,b). Finally, delay-Doppler radar images of near-Earth asteroids (Ostro 1993) reveal bizarre shapes that may have resulted from tidal distortion during close encounters with Earth (Bottke *et al.* 1997b???): asteroids 1769 Castalia, 4179 Toutatis, and 2063 Bacchus look like dumbbells, while 1620 Geographos has a highly elongated porpoise-like profile.

In this paper, we will investigate whether the tidal field of the Earth is responsible for some or all of these phenomena. We use a direct *N*-body model which simulates close encounters of rubble-pile progenitors with the Earth. After characterizing various types of tidal disrupiton regimes, we compare our results to the observations outlined above. Our conclusions indicate that tidal disruption must now be considered an important mechanism for understanding the evolution of ECAs and other near-Earth objects.

1.2 Previous Work on Tidal Disruption

Boss *et al.* (1991) stated that most of the literature on tidal processes can be divided into two broad, sometimes overlapping categories: "tidal failure", where a body with material strength undergoes tidal stresses until fracture and/or failure is induced, and "tidal disruption", where a body is separated into two or more fragments whose orbits diverge following a planetary encounter. Here we briefly review the papers which concentrate on tidal disruption.

Roche (1847; see Chandrasekhar 1969) showed that a self-gravitating synchronously-rotating liquid satellite circling a spherical planet cannot keep an equilibrium figure inside a critical distance

$$R_{\rm Roche} = 1.52\left(\frac{M_{\rm pl}}{\rho_{\rm sat}}\right)^{1/3} \approx 2.46 R_{\rm pl}\left(\frac{\rho_{\rm pl}}{\rho_{\rm sat}}\right)^{1/3}, \qquad (2)$$

where M_{pl}, R_{pl}, and ρ_{pl} are the mass, radius, and density, respectively, of the planet, and ρ_{sat} is the density of the satellite. Thus, a strengthless body with a density of 2 g cm^{-3} disrupts only if it orbits the Earth at a distance less than $3.4\ R_{\oplus}$, where $R_{\oplus}$ is the Earth's radius.

Jeffreys (1947) and Öpik (1950) applied these ideas to calculate the tidal stress induced inside a solid satellite. Comparing those values to the strength of rock (e.g., asteroids and rocky satellites) and ice (e.g., comets and icy satellites), they concluded that tidal disruption of solid objects in the solar system was unlikely to occur unless the satellite was unusually large and close to a planet. Both predicted that the rings of Saturn could not have been formed by the tidal disruption of a solid satellite. Including the satellite's self-gravity into the theory, however, Öpik (1966) demonstrated that tidal forces should be important for bodies with weak internal structures (e.g., comets). Öpik even suggested that comet Ikeya Seki, which broke up during its close approach to the Sun in 1965, may have had a "rubble-pile" structure.

Sekiguchi (1970) examined whether lunar tides were strong enough to distort or disrupt asteroids before impact, in the hope that they might explain many of the more unusual craters on the Moon's surface. Though he was the first to consider non-orbital trajectories for his progenitors, several errors have now been found in his technique, making his interpretations questionable (Dobrovolskis 1990). Aggarwal and Oberbeck (1974) later expanded on Sekiguchi's work to investigate various modes of fracture in elastic impactors and orbiting satellites.

Dobrovolskis (1982) modeled tidal fracture in a homogeneous triaxial ellipsoid and applied his model to Phobos and other bodies. His results indicated that Martian tidal forces are attempting to "squash" Phobos along its long axis, but that it is stable at its present distance from Mars.

Mizuno and Boss (1985) used a numerical grid-based hydrocode with viscosity to study the tidal disruption of 1000-km planetesimals passing by an Earth-sized planet on a parabolic trajectory. Their results showed that internal dissipation can prevent tidal disruption, even when the planetesimals are on near Earth-grazing trajectories. Kaula and Beachey (1984), using a related method, found similar results. Dobrovolskis (1990) and Sridhar and Tremaine (1992), however, questioned whether the dissipation model used by Boss *et al.* (1991) was realistic: actual planetesimals, they argued, may not be strongly dissipative. To emphasize this point, Dobrovolskis (1990) examined how realistic failure affected tidal disruption in homogeneous objects composed of both ductile (e.g., iron) and brittle (e.g., stone or ice) materials. His results set strict limits on the size, strength, material properties, and orbital parameters required to produce a break-up event.

Melosh and Stansberry (1991), while investigating the formation of doublet craters on Earth, tested whether contact-binary asteroids (i.e., two-component rubble-piles) could be pulled apart by tidal stresses just prior to impact. They found that this scenario, in general, only causes separation in a direction along the impact trajectory, such that the binary components tend to strike very close to one another. Related papers by Farinella (1992), Farinella and Chauvineau (1993), and Chauvineau *et al.* (1995) investigated the effects of planetary tides on binary asteroids. They found that close encounters modify the separation distance between the components, frequently increasing their mutual semimajor axis and eccentricity. Accordingly, strong perturbations often cause binary components to collide or escape one another.

Boss *et al.* (1991), using a "smooth particle hydrodynamics" (SPH) model, explored whether non-rotating, self-gravitating, inviscid planetesimals encountering the Earth suffer tidal disruption. They found that large ($0.1\ M_{\oplus}$) planetesimals remain intact, mostly because their size limits the approach distance. Small ($0.01\ M_{\oplus}$) planetesimals were found to disrupt when their encounter velocities (v_{∞}) were less than 2 km s^{-1} and their close approach distances (q) were less than $1.5\ R_{\oplus}$ from the center of the Earth. Boss *et al.* also discovered that Earth's tidal forces induce elongation and spin-up in the planetesimal; this effect actually causes the observed mass-shedding in many cases. Interestingly, some of their test cases revealed SL9-like outcomes nearly two years before the discovery of SL9 itself.

Sridhar and Tremaine (1992) developed an analytical methodology to ascertain how non-rotating, self-gravitating, viscous bodies undergo tidal disruption. They showed that such bodies shed mass if their periapse is smaller than:

$$R_{\mathrm{disrupt}} \simeq 0.69 R_{\mathrm{Roche}} = 1.05 \left(\frac{M_{\mathrm{pl}}}{\rho_{\mathrm{pro}}}\right)^{1/3} \simeq 1.69 R_{\mathrm{pl}} \left(\frac{\rho_{\mathrm{pl}}}{\rho_{\mathrm{pro}}}\right)^{1/3}, \qquad (3)$$

where ρ_{pro} is the body's density (i.e., the same parameter as ρ_{sat} from Eq. (2)). Their results, like Boss *et al.* (1991), showed that weak objects can undergo SL9-type disruptions. Lacking the ability to include vorticity in their model, however, Sridhar and Tremaine were unable to look into tidal spin-up mechanisms.

Watanabe and Miyama (1992) modelled the tidal interactions between inviscid planetesimals of comparable size. Though their results focussed on effects occurring near or during collisions, they did find that tidal forces yield important effects when the planetesimals' relative encounter velocity is less than their mutual escape velocity.

Asphaug and Benz (1994; 1996), along with several other groups (e.g., Boss 1994; Rettig *et al.* 1994; Sekanina *et al.* 1994) investigated the tidal disruption of SL9 using numerical codes. We focus on the results of Asphaug and Benz (1996), however, since their extensive test results provide a good fit to observational constraints, and because their methods are germane to the issues contained in this paper. Using an SPH code similar to that used by Boss *et al.* (1991), Asphaug and Benz (1996) tested two types of cometary progenitors: a non-rotating solid sphere and a non-rotating spherical rubble-pile of equal-sized particles. In the former case, they found that solid comets fracture and split under tidal stresses in binary fashion, regardless of the comet's material properties. This hierarchical splitting (i.e., 2 pieces, 4 pieces, 8 pieces, etc.) was considered too slow and difficult to create the more than 20 roughly equal-sized fragments comprising SL9. A better match was found with the rubble-pile model. Using SL9's orbital constraints, they found Jupiter's tidal forces could pull the pile into an elongated needle-like structure which, as it receded from Jupiter, clumped into multiple equal-sized fragments.

Bottke and Melosh (1996a,b) investigated how rotating contact-binary asteroids might disrupt during close approaches with Earth and other terrestrial planets. They found that tidal forces frequently cause these bodies to undergo fission, pulling them into separated components which can begin to orbit one another. Their results suggested that as many as 15% of the km-sized Earth-crossing asteroids may have binary companions produced by this mechanism, enough to explain the large fraction of doublet craters seen on Earth (~10%). Comparisons with the doublet crater populations on Venus (Cook *et al.* 1997) and Mars (Melosh *et al.* 1997) also yielded good matches.

Solem and Hills (1996) investigated how Earth's tidal forces might modify the shapes of many Earth-crossing asteroids. Using a non-rotating spherical aggregate as their progenitor, they found that close Earth approaches often kneaded the body into an elongated shape reminiscent of highly elongated asteroids such as 1620 Geographos.

NEED CONCLUDING/TRANSITION PARAGRAPH???

2 METHOD

2.1 Tidal Disruption Model

The rubble-piles in our simulations are qualitatively similar to those used previously by Asphaug and Benz (1996) and others: they are roughly the same size, they have approximately the same number of particles, and they are only held together by self-gravity. Specifically, our progenitor is an aggregate of 247 identical spherical particles, each 255 m in diameter. The number of particles was chosen as a compromise between resolution and computation time: each individual run takes several hours to complete on a 200 MHz Pentium running Linux. In order to make our simulations more realistic than previous efforts, however, we have introduced several enhancements:

1. Non-sphericity. We investigated two different configurations for our rubble-piles: a nearly spherical progenitor like those used by Asphaug and Benz (1996) and an ellipsoidal progenitor which more closely resembles real Earth-crossing objects (McFadden *et al.* 1989; Ostro 1993; Ostro *et al.* 1995a,b). For the latter case, the body was given dimensions of $2.8 \times 1.7 \times 1.5$ km ($1.8 \times 1.1 \times 1.0$ normalized), not unlike the axis ratio of 4769 Castalia (Hudson and Ostro 1995a). We chose the elongated shape because spherical progenitors (used by all other groups) have lower [illegible] potential energies, making them intrinsically stable against tidal disruption than other configurations.
2. Rotation. We let our progenitors rotate over a range of spin periods and spin axis orientations. Our spherical progenitor was tested for spin periods of $P = 6$ h, while our elongated progenitor was tested for $P = 4, 6, 8, 10, 12$ h, and $P = \infty$ (i.e., no spin). Most earlier models used progenitors without spin since (a) it is simpler, and (b) objects with random spin axis orientations have a nearly equal probability of encountering a planet with a prograde or retrograde spin, making the "zero spin" case a reasonable representative case. This "average" progenitor ($P = \infty$), however, does not necessarily produce the median break-up outcome. Our results indicate that the median break-up outcome is instead dominated by objects with prograde spins, which are susceptible to tidal disruption (note unpublished work by Asphaug and Benz shows this same result).
3. Hyperbolic flybys. Planar hyperbolic encounters can be defined by the rubble-pile's encounter velocity at "infinity" (v_∞, the velocity of a body before the gravitational acceleration of Earth becomes significant) and its periapse distance (q). Previous models usually simulated parabolic encounters ($v_\infty \equiv 0$). Such trajectories provide a useful approximation, but they are not as representative as hyperbolic trajectories ($v_\infty > 0$).
4. Friction or energy dissipation. Collisional energy loss is incorporated through a coefficient of restitution ϵ (i.e., the ratio of the rebound speed to the impact speed). For the cases in this paper, $\epsilon = 0.8$. Our tests show tidal disruption is largely insensitive to the choice of ϵ so long as collisions are inelastic ($\epsilon < 1$) (also seen by E. Asphaug, personal communication). Previous models featured only elastic collisions.

The bulk density of our rubble-piles was set to 2 g cm^{-3}. Individual particles were given densities of 3.6 g cm^{-3}, similar to ordinary chondritic meteorites (Wasson 1974). Our choice of bulk density may be conservative, given the estimate of 253 Mathilde's bulk density (1.3 g cm^{-3}), but it is reasonable given the range of densities measured for Phobos and Deimos (~ 2 g cm^{-3}; Thomas *et al.* 1992) and 243 Ida (between 2.1 and 3.1 g cm^{-3}; Belton *et al.* 1995). We have decided to omit test runs with cometary bulk densities in this paper for computational expediency and because we do not expect many comets to tidally disrupt near the Earth. Long period comets typically have such high encounter velocities with Earth (the mean encounter velocity is ~ 55 km s^{-1}; Weissman 1982) that few are expected to undergo tidal disruption, despite their lower bulk density and hence larger Roche sphere. The contribution of short-period comets to the near-Earth object population is thought to be negligible (Morrison 1992). We chose not to address the issue of extinct comets within the Earth-crossing asteroid population at this time.

2.2 Complications Using Rotating Elongated Rubble-piles

Allowing rubble-piles to rotate significantly increases the complexity of the simulation and the size of parameter space that must be investigated to adequately characterize tidal disruption outcomes. For example, an object that disrupts during a close approach when rotating prograde (i.e., in the same sense as the orbit) may not disrupt if the spin is retrograde. Our results will show that the quantity of mass shed during a disruption event varies according to the orientation of the body's spin axis at periapse with the Earth (perigee).

We define this orientation using two angles: α, the angle between the rotation pole and the normal of the progenitor's orbit plane (analogous to the obliquity of a planet), and β, the projected angle between the pole and the vector connecting the progenitor with the center of the Earth at perigee, measured in the orbital plane (Fig. 1). Thus, prograde spins have $\alpha < 90°$, while retrograde spins have $\alpha > 90°$.

Use of a non-spherical progenitor also complicates matters. We find that the orientation of the body's long axis at perigee affects the amount of mass shed during tidal disruption. Consequently, we keep track of the rubble-pile's rotation phase, using the angle θ (Fig. 1). When $\theta = 0°$, the long axis (or its projection in the orbit plane) points directly toward the Earth. When $\alpha < 90°$ (prograde rotation) and $0° \leq \theta \leq 90°$, the leading long axis of the object is rotating toward the Earth just before close approach. Conversely, when $\alpha < 90°$ (prograde) and $90° \leq \theta \leq 180°$, the leading long axis is rotating away from the Earth.

2.3 Description of Numerical Technique

The numerical code and methods described here are largely based on Richardson (1993; 1994; 1995). All computations take place in three dimensions and there is no limit to the spatial domain that can be occupied by the particles. We use a direct method for integrating the equations of motion that arise from particle self-gravity. Although this method scales as N^2, where N is the number of particles in the rubble-pile, we use relatively few particles ($\lesssim 1000$) so that there is little advantage to employing cost-reducing algorithms such as tree codes. A typical run with our 247-particle aggregates involves over half a million collisions in about 5 million timesteps.

Our numerical integrator is a 4th-order predictor-evaluator-corrector scheme that features *individual* particle time-steps (Aarseth 1985). The individual steps are critical in order to detect collisions accurately (Richardson 1994). In addition, the force and first three time derivatives yield a very sensitive timestep criterion (Press & Spergel 1988). It should be emphasized that collisions between particles are detected only *after* they have taken place. That is, collisions are detected by noting whether there is overlap between the current particle and its nearest neighbor. For the bulk of the runs discussed here, the timestep coefficient was chosen such that overlaps are typically no greater than 0.1% of the sum of the radii of the colliding pair. This parameter choice has been found to conserve angular momentum adequately (< 5% deviation) over the course of a typical rubble-pile asteroid encounter with the Earth. Encounters completed with smaller timestep coefficients (i.e., greater accuracy at the cost of computational efficiency) show no significant differences. For our simulations, all particles are modeled as indestructible uniform spheres. The particles lack sticking forces, such that agglomeration arises solely from self-gravity.

As mentioned previously, each model incorporates a normal coefficient of restitution $\epsilon = 0.8$. There is no surface friction in the models (i.e., the transverse restitution coefficient is unity). Without radial damping, any clumps that form by gravitational instability are noticeably less tightly bound. For collisions at small relative speeds however ($v \lesssim \frac{1}{3} v_{\mathrm{esc}}$, where $v_{\mathrm{esc}} \sim 18$ cm s^{-1} is the surface escape speed of a particle in our simulation), it is necessary to adopt $\epsilon = 1.0$ to prevent computationally expensive surface sliding motions (Petit & Hénon 1987). A minimum time-step δt_{min} of 10^{-10} time units (one time unit = $1/2\pi$ yr) is imposed to ensure that time-stepping does not venture too close to the limits of machine precision. Also, a maximum step of 0.01 time units is used to ensure a minimum integration accuracy for particles that have drifted far from their perturbing neighbors. For additional details regarding the precise calculations needed to handle collisions in a dense self-gravitating environment such as a rubble-pile, see Richardson (1994).

It is interesting to note that our rubble-piles have some fluid-like properties, especially at the moment of disruption. That is, the rubble-pile is seen to flow viscously from one form to another during disruption. Indeed, it has been found that under some circumstances (usually after free-fall accretion), a rotating rubble-pile has a shape consistent with a Jacobi ellipsoid (*cf.* Binney and Tremaine 1987). However, not all rubble-pile configurations are Jacobi ellipsoids, a fact which appears to be due to the rubble-pile's granular nature. Thus, the rubble-pile can get trapped in a local energy minimum that requires a finite input of energy before the material can reconfigure itself through dissipation into a lower energy state. This effect is similar in concept to the angle of repose of granular media, a quantity that depends only on the material characteristics of the grains. Because of this, our progenitors generally maintain their shapes prior to Earth encounter despite being given different initial rotation rates. Friction also makes our rubble-piles slightly more difficult to disrupt than the more fluid objects studied by Sridhar and Tremaine (1992), though we believe it also causes our bodies to behave more like real comets and asteroids.

To minimize round-off error when particle separations are computed, we carry out the simulations in the rubble-pile's center-of-mass frame. The equation of motion for the i-th particle is then written:

$$\ddot{\mathbf{r}}_i = \mathcal{F}_i - \frac{GM_\oplus}{R_{i\oplus}^3}\mathbf{R}_{i\oplus} \qquad (4)$$

where

$$\mathcal{F}_i = -\sum_{j\neq i} \frac{Gm_j}{|\mathbf{r}_i - \mathbf{r}_j|^3}(\mathbf{r}_i - \mathbf{r}_j) \tag{5}$$

is the force per unit mass on the ith particle due to the Earth and the other rubble-pile particles. The second term in Eq. (4) represents the acceleration of the center-of-mass frame by the Earth and is calculated to high order in the position vector. Note that in this model, the force contribution of the Earth is treated like that from any other point-mass particle (i.e., in the summation, $m_0 \equiv M_\oplus$, $\mathbf{r}_0 \equiv \mathbf{R}$ and shape effects are ignored), although the back-reaction of the rubble-pile particles on the Earth is neglected. Also, neither the tidal effect of the Sun nor the perturbing effect of the Moon have been included in these calculations. As we are primarily interested in the mechanics of tidal breakups, such slow-acting perturbing effects can be ignored.

The starting distance of the asteroid from the Earth is 15 Roche radii (recall $R_{\rm Roche} \sim 3.4\ R_\oplus$ for a body with bulk density $\rho_{\rm bulk} = 2$ g cm^{-3} in the vicinity of the Earth), large enough to ensure planetary perturbations are negligible at the outset, but small enough to make exploration of parameter space practical. Each run is terminated at a post-encounter distance of $\sim 60R_\oplus$, the distance between the Earth and the Moon. See Appendix A for a derivation of the total integration time for these orbits, parameterized by the close approach distance q and the encounter velocity v_∞.

During the run, periodic outputs are generated: summary statistics for diagnostic purposes, particle positions and velocities for analysis such as clump identification, and animation frames. Also recorded is the instant of closest approach (periapse passage) for follow-up determination of the asteroid orientation at the point of maximum tidal stress.

2.4 Analysis Method

2.4.1 Clump-finding algorithm

The most basic information that can be gleaned from a tidal encounter is the nature and amount of any shed material. Our analysis code automates the categorization of each tidal encounter by identifying the post-encounter distribution of particles. The largest (most massive) clump is taken to be the progenitor's *undisrupted remains*. The outcome classes, which we define in Section 3.1, are simply determined by the mass fraction of these remains.

To find clumps, we define a "radius of influence":

$$\mathcal{R} = \max(0.1 R_{\rm Hill},\ n_c^{1/3} \ell_{\rm max}), \tag{6}$$

where

$$R_{\rm Hill} = r\left(\frac{m_c}{3M_\oplus}\right)^{1/3} \tag{i}$$

is the Hill radius (the characteristic distance of influence in the restricted three-body problem; here m_c is the clump mass and r is the distance of the progenitor center of mass from the Earth), $\ell_{\rm max}$ is the maximum dimension of the clump, and n_c is the number of particles in the clump. Eq. ((i) was arrived at through trial-and-error and by comparing the computed clumps with a visual examination of the data. Although largely empirical in origin, it has been found that use of this formula in the clump finding algorithm results in a very high detection accuracy percentage. The use of the max() function strikes an excellent balance between gravitational association (via the Hill radius) and physical proximity.

Initially Eq. (6) is used to find the radii of influence of individual particles (i.e., in the formula, $n_c = 1$, m_c is the particle mass, and $\ell_{\rm max}$ is the particle radius). Each particle is checked in turn to see whether there are any overlaps between spheres of influence. If an overlap is detected, the particles are merged together to form an "association" or "proto-clump". The algorithm then proceeds iteratively, first recalculating radii of influence for any new associations created, then checking overlaps for all particles and associations, until after a complete pass there is no change in association membership. Once this procedure terminates, any associations with three or more particles are considered to be clumps.

Comparisons between the algorithm's results and a visual examination of outcomes have yielded favorable matches in nearly all cases. In addition, this simple clump-finding routine was compared with the output from SKID (Stadel *et al.*, in preparation)[3], a generalized code developed for cosmological simulations that finds gravitationally bound groups in N-body simulations by following density gradients and using the "friends-of-friends" technique. There was no significant difference in detection accuracy found between the two methods.

---

[3] The code is publicly available from `www-hpcc.astro.washington.edu/tools/SKID/`.

2.4.2 Properties of the post-encounter remnant

Once the clumps have been identified, the most massive clump is taken to be the remnant of the original rubble-pile. The following properties are then measured:

1. Mass. To determine the relative mass of the remnant, we take the ratio of the number of particles in the clump to the total number of particles in the simulation (N). Since all particles are identical, this yields the remnant's mass fraction $M_{\rm rem}$.

2. Rotation period. To determine the rotation period, $P_{\rm rem}$, we first compute the inertia tensor $\mathbf{I}$ of the clump, given by:

$$\mathbf{I} = \sum_i \left[\mathbf{I}_i + m_i(r_i^2\mathbf{1} - \mathbf{r}_i\mathbf{r}_i)\right] , \tag{8}$$

   where $\mathbf{I}_i = \frac{2}{5}m_iR_i^2\mathbf{1}$ is the inertia tensor of each constituent particle i (m_i is the particle mass and R_i the radius; $\mathbf{1}$ is the unit matrix), and $\mathbf{r}_i$ is the particle position relative to the clump center of mass. Next, the angular momentum of the clump with respect to its mass center is computed according to:

$$\mathbf{h} = \sum_i m_i\mathbf{r}_i \times \mathbf{v}_i , \tag{9}$$

   where $\mathbf{v}_i$ is the particle velocity relative to the clump center of mass. Note that intrinsic particle spin is ignored since the coefficient of surface friction is unity in all models. Now, since for a solid body, $\mathbf{h} = \mathbf{I}\boldsymbol{\omega}$, where $\boldsymbol{\omega}$ is the clump angular velocity, the rotation period of the clump is given by:

$$P_{\rm rem} = \frac{2\pi}{|\boldsymbol{\omega}|} = \frac{2\pi}{|\mathbf{I}^{-1}\mathbf{h}|} \tag{10}$$

   Note that this formalism assumes that the clump can be treated as a rotating solid body (i.e., one in which the position vectors $\mathbf{r}_i$ remain fixed in the body frame). In the presence of shear (such as during the actual disruption event when particles closer to the planet acquire a larger Keplerian speed than those further away), some outer particles may rotate slower about the mass center than the solid body rate of the core, giving rise to a somewhat longer period. This factor, however, does not appear to affect our results in any significant way since spins are generally measured well after disruption.

3. Clump dimensions. The inertia tensor is also used to calculate the clump dimensions (including the quantity $\ell_{\max}$ used in the iterative procedure described above). First, the principal axes of the clump are obtained by diagonalizing the inertia tensor and solving for the eigenvectors (e.g., Press *et al.* 1992, §11.1–11.3). This procedure, however, only provides the body axis orientations, not the lengths. To compute the lengths, all possible two-body particle separations are calculated and projected onto each body axis. The largest separations a_1, a_2, and a_3 along each axis are recorded and sorted so that $a_1 \geq a_2 \geq a_3$. These are taken to be the clump dimensions (so $\ell_{\max} \equiv a_1$). Note that distances between spheres along a given axis include the finite size of the spheres (i.e., $2R_i$ is added to each length). In the literature, the axis ratios $q_2 \equiv a_2/a_1$ and $q_3 \equiv a_3/a_1$ are often used to characterize non-axisymmetric bodies such as these clumps. In addition, we define a convenient single-value measure of the body's "ellipticity" using the quantity $\varepsilon_{\rm rem} \equiv 1 - \frac{1}{2}(q_2 + q_3)$.

4. Phase angle of long axis at periapse. The orientation of the rubble-pile's long axis at periapse θ is derived from the principal axes of the inertia tensor. The magnitude of θ depends on the angle between the body major axis and the position vector of the planet. The sign of θ is governed by the relative orientation of the body major axis with the rubble-pile's velocity vector. Thus, if $\mathbf{p}_1$ is the major axis vector of the rubble-pile, and $\mathbf{r}$ is the position of the Earth with respect to the rubble-pile's center of mass, then the phase angle θ can be found by taking the dot product between them:

$$\theta = \begin{cases} \cos^{-1}(\hat{\mathbf{p}}_1\cdot\hat{\mathbf{r}}) & \text{if } (\hat{\mathbf{p}}_1\cdot\hat{\mathbf{v}}) \leq 0 \\ \pi - \cos^{-1}(\hat{\mathbf{p}}_1\cdot\hat{\mathbf{r}}) & \text{otherwise} \end{cases} , \tag{11}$$

   where $\mathbf{v}$ is the velocity of the Earth with respect to the rubble-pile's center of mass, and ^ denotes the unit vector. Our coordinate system is oriented so that at periapse, $\mathbf{r}$ points in the negative x-axis direction and $\mathbf{v}$ points in the negative y-axis direction. Note that there is an ambiguity of π in the orientation of $\mathbf{p}_1$.

2.4.3 Osculating elements

Finally, to categorize the material liberated from the progenitor, we determine the mass fraction of clumps that are in the process of escaping, orbiting, or reaccreting onto the remnant rubble-pile. These *ratios* are derived by computing the osculating elements of all the other clumps with respect to the remnant. A reaccreting clump is one for which the orbital eccentricity with respect to the remnant rubble-pile is $e < 1$ and for which the semi-major axis $a \leq \ell_{\max} + a_1$, where a_1 is the length of the longest body axis of the clump in question. Otherwise, if $e < 1$, the clump is considered to be orbiting the remnant rubble-pile. If $e \geq 1$, *the clump is escaping*. The total number of particles in each category is divided by N to form the ratios.

The equations for a and e are similar to those found in Appendix A. For completeness, the orbital inclination is given by $i = \cos^{-1}(\hat{\mathbf{h}} \cdot \hat{\mathbf{h}}_0)$, *where* $\mathbf{h}$ *and* $\mathbf{h}_0$ *are* the relative angular momenta of the clump with respect to the remnant, and the remnant with respect to the planet, respectively.

3 RESULTS

3.1 Tidal Encounter Outcome Classes

In the course of performing our simulations we found that differences in tidal encounter outcomes could be divided into four broad but distinct classes. These qualitative morphological differences are well correlated with a simple parameter, the post-encounter mass fraction of the progenitor (M_{rem}). The classes are:

1. Catastrophic or "S" disruption ("S class"). We classify the disruption as S class when the largest remaining fragment retains less than 50% of the progenitor's original mass (Fig. 2a). For this most dramatic outcome class, the equipotential surface (which is everywhere perpendicular to the local gravity, including tidal and centrifugal terms) of the rubble-pile asteroid is stretched into a spindle-like shape pointing toward and away from the planet at close approach. Particles outside the new equipotential surface move "downhill" to fill in that shape, though friction and the particles' own inertia prevent them from arriving at their new positions instantaneously. As the rubble-pile recedes from the planet, it continues to stretch apart while gravitational instabilities along the length gradually cause particles to clump into a number of roughly equal-sized bodies. This disruption type is analogous to that seen when comet SL9 was pulled apart near Jupiter (*cf.* Section 1).

   [MORE INFO NEEDED IN THIS PARAGRAPH] We find that the debris train length L grows almost linearly following S class disruptions (Fig. 3), as is expected for hyperbolic encounters (Hahn, private communication), in contrast to the $t^{1/3}$ asymptotic growth mode of parabolic models (e.g., Sridhar and Tremaine 1992). If the fundamental wavelength of the gravitational instability λ is known, the number of clumps expected is simply given by the ratio L/λ at some characteristic time (e.g., free-fall time) following disruption. It has been found that a simple Jeans approximation to λ provides a reasonable match to disruptions within this class. More work is needed to generalize the theory to other disruption end states (Hahn, in preparation).

2. Rotational break-up (B-class). We classify the disruption as B class when the largest remaining fragment retains between 50% and 90% of its mass (Fig. 2b). With this less violent form of disruption, the consequence of the imbalance between the Earth's gravitational pull and the extra centrifugal force acting on the rubble-pile as a result of the orbital motion is more clearly seen. The end of the body nearest Earth experiences an excess of gravitational force pulling it radially toward the planet, while the end of the asteroid furthest from Earth experiences an excess of centrifugal force pulling it radially away from the planet. The difference results in a torque which pulls the asteroid's long axis toward a radial line stretching from the asteroid's center of mass to the Earth's center. In many cases, tidal torque increases the rubble-pile's length and accelerates its rotation rate (Boss *et al.* 1991; Boss 1994; Solem and Hills 1996). In a B class outcome, the torque is strong enough to cause particles or clumps near the ends of the rubble-pile to be thrown into space in the asteroid's equatorial plane PROGRADE ONLY???. The initial spiral patterns thus produced are similar to those seen in models of stellar collisions (Benz and Hills 1987; Benz *et al.* 1989). The material shed during this process often removes enough angular momentum from the rubble-pile to slow the remnant's rotation below the pre-encounter rate.

3. Mild disruption (M-class). M class disruptions are those for which the stripped material accounts for less than 10% of the progenitor's mass (Fig. 2c). In this case only small clumps or individual particles at the limit of the model resolution are lost. However, in the process, the progenitor shape is often strongly distorted. Also, our simulations typically show that in these borderline cases the end of the rubble-pile swinging by Earth near perigee suffers more elongation and mass shedding than the far end. Thus, the near end becomes long and tapered, while the far end remains more stout. In some cases, these ends also retain small cusps swept back against the direction of rotation, like a pinwheel. This shape resembles at least one near-Earth asteroid imaged by delay-Doppler radar techniques (*cf.* Section 4.1). The asymmetry of the tidal distortion may be due to finite-particle effects.

4. No mass loss (N-class). For this outcome class, no mass is lost during the encounter but tidal torques may still reshape the asteroid and/or change its spin rate (Fig. 2d).

3.2 Dependance on Model Parameters

There are many physical parameters that determine the tidal encounter outcome: the trajectory (two parameters; more if planet shape effects are included), the rotation rate (one parameter), the spin axis orientation (two parameters), the body shape and overall size (at least three parameters), the long axis orientation at periapse (one parameter), the planet/body density ratio (one parameter), the nature of the constituent rubble-pile particles (many parameters), etc. There are evidently far too many parameters to explore all of them in systematic fashion, so we fix the least crucial and vary the most important, the latter being the trajectory, rotation, shape, and density ratio.

3.2.1 Trajectory: Varying q and v_∞

For these tests we chose Earth as the target and used our "generic" elongated asteroid with perfectly prograde rotation ($\alpha = 0^\circ$; no spin-axis tilt). The spin period was set to 6 h, the median rotation period of Earth-crossing asteroids (Harris 1996). The phase angle θ was constrained to lie between 0° and 90° in order to encourage tidal disruption (*cf.* Section 2.4 and discussion on θ below).

Since tidal forces vary as the inverse cube of the distance, we expect that the perigee q is one of the most important parameters in tidal breakup. Our results confirm this strong dependence (Fig. ??): as q increases from 1.01 to 3.8 $R_\oplus$, tidal disruption becomes more difficult and less violent, changing the outcome from S class for the smallest q values, through B and M class for intermediate values, and finally to N class for the largest q values. To illustrate this further, Fig. 6 shows the configurations of the $P = 6$ h rubble-piles at the termination of their runs. Both plots indicate that even at the slowest encounter speeds, there is a distance beyond which mass stripping no longer takes place. Naturally this limit is related to the Roche limit (Eq. (2)).

The encounter velocity (v_∞) is also of critical importance. As the encounter speed v_∞ increases from 3 to 24 km s^{-1}, tidal disruption again becomes less violent. Faster encounter speeds mean less time spent near the Earth where tidal forces are strongest. If v_∞ is sufficiently high, no q value will allow disruption. Our results indicate that this limit is well below the average encounter speeds of comets with the Earth (~ 55 km s^{-1}; Weissman 1982). Thus, we predict that few comets ever undergo tidal disruption in the terrestrial planet region.

In general, we find a qualitative inverse relationship of outcome on q and v_∞. Again this is related to the penetration distance inside the Roche sphere and the time spent within the sphere: the closer the penetration point to the planet, the larger the range of encounter velocities that can lead to disruption. Accordingly, this relationship applies most strongly for S class events and less so for B and M class events.

As an aside, we caution that these results suffer to a limited extent from unavoidable discreteness effects, arising both from the practical limitations of exploring parameter space with infinite resolution and from the complications introduced by variations in θ (discussed below). This discreteness should be kept in mind when interpreting the results.

3.2.2 Rotation speed: Varying P

Rotation also strongly affects tidal breakup. For that reason, we devote considerable effort to exploring it with greater range and resolution than previous studies. We have examined $P = 4$, 6, 8, 10, and 12 h for prograde rotation with no spin axis tilt, as well as the no-spin ($P = \infty$) case. Fig. 4 summarizes these results. The plots have been scaled with respect to one another to indicate the relative sizes of the q-v_∞ space explored in each case.

Generally, faster rotation enhances disruption, increasing the range of q and v_∞ values for which S, B, and M class disruptions occur. Within the discreteness limits of the plots, the area encompassed by mass-loss classes shrinks as the rotation period increases. Note however the difference in outcomes between $P = 4$ h and $P = 6$ h is greater than the difference between $P = 10$ h and $P = 12$ h. This effect is not surprising, since the former cases are much closer to the rotational break-up limit given in Eq. (1) than the latter cases (3.1 h for our rubble-piles). Since a particle at the tip of one of our $P = 4$ h rubble-piles moves at $\sim 70\%$ of escape velocity, only a small increase in rotational momentum from tidal forces is needed to eject the particle into space. If the rubble-pile rotated more slowly, say at $P = 12$ h, the same particle (now moving at $\sim 25\%$ the escape velocity) would require a bigger kick from tidal forces for ejection. Even objects without spin ($P = \infty$), however, undergo tidal disruption if q and v_∞ are small enough, as seen in the Figure.

3.2.3 Spin axis orientation: Varying α and β

The direction of the rubble-pile's spin axis also plays a role in tidal breakup. So far we have only shown pure prograde cases ($\alpha = 0^\circ$), though retrograde ($\alpha = 180^\circ$) and intermediate obliquity cases (with $0^\circ < \alpha < 180^\circ$ and $0^\circ \le \beta < 360^\circ$) evidently must occur as well. In fact, intermediate obliquities are statistically more probable than pure prograde or retrograde spin, for any given encounter. Unfortunately, they also comprise a very large portion of parameter space. Thus, for computational expediency, we have limited our investigation of α and β to a representative S class event ($P = 6$ h, $v_\infty = 6$ km s^{-1}, and $q = 1.4\ R_\oplus$) and B class event (same P and v_∞ but $q = 2.2\ R_\oplus$).

Fig. 7 shows the effect of varying the rotation angles α and β for these cases. The rotation pole angle α was varied between 0° and 180° in steps of 30°. The rotation axis was constrained to lie along the xz-plane ($\beta = 0°$ and 180°) or yz-plane ($\beta = 90°$ and 270°). Computational constraints prevented systematic testing of additional angle combinations, though the other values of β we did test yielded results between these extremes.

From the Figure, parameters that produce an S class event when $\alpha = 0°$ continue to produce outcomes with strong mass loss so long as the rubble-pile's rotation is prograde (i.e., $\alpha \leq 90°$). The severity of mass shedding within a class, however, decreases somewhat as α approaches 90°. For example, the B-class event in the same figure changes to an M-class event as α increases. Once rotation becomes retrograde ($\alpha > 90°$), mass shedding is strongly suppressed. Note that the transition is not as rapid when the rotation axis is confined to the yz-plane ($\beta = 90°$ and 180°). This is because the long axis of the body continues to sweep towards and away from Earth, allowing the large moment arm to assist the breakup. We also caution that these outcomes have been influenced by noise in θ: the rough symmetry seen in between S, B, M, and N class runs for $\beta = 0°, 90°$ and $\beta = 90°, 270°$ is real. WHAT DOES THIS MEAN???

We have also examined pure retrograde spin cases ($\alpha = 180°$) for various values of q and v_∞. Our results show that rubble-piles with spin periods of $P = -6$ h are nearly immune to tidal disruption, regardless of their trajectories. Milder $P = -12$ h runs were also performed (Fig. 8; compare with Fig. 4). Although the range of disruption outcomes over q and v_∞ is greatly reduced compared to the prograde case, note that all four outcome classes are still seen. Slowly rotating rubble-piles have relatively little angular momentum, so they are about as difficult to disrupt as objects without spin, and such $P = \infty$ objects still show S class outcomes (Fig. 4). Note however that as the retrograde spin increases, S class outcomes become more and more suppressed.

3.2.4 Long axis orientation: Varying θ

The effectiveness of tidal disruption also depends on θ, the rotational phase of the rubble-pile's leading long axis at perigee. Our runs show that when the leading long axis is rotating towards the Earth in the prograde sense, tidal torque and centrifugal force work together to enhance disruption. When the leading long axis is rotating away from the Earth, tidal torque and centrifugal force oppose one another to deter disruption. Recall that tidal forces near perigee stretch the shape of the equipotential surface of the body in the direction of the Earth; particles move "downhill" to fill that shape if they can. When $90° < \theta < 180°$, however, this movement is opposed by rotation, which often causes the particles to collapse back to the remnant rubble-pile, typically making the shape more spherical. This is similar to what happens to a rubble-pile with retrograde spin.

Since we need θ between 0° and 90° to achieve tidal disruption, we try to "aim" the initial phase angle of the body to reach $\theta \sim 15°$. Unfortunately it is difficult to constrain a given run to use a particular value of θ. The reason for this is three-fold: (1) torquing effects close to perigee that depend on the orientation angle often change the rotation rate; (2) there is a slight adjustment (contraction or expansion) that depends on the initial rotation period; and (3) there is a small secular increase in angular momentum that is an unavoidable but controllable consequence of the numerical collision algorithm (controllable in the sense that as the time-steps are forced to be smaller the spurious spin-up also decreases in severity). In practice spin changes do not exceed 5% of the initial value, but nevertheless the effect makes it difficult to constrain θ exactly. More precise runs can be made, but only at the expense of increased CPU time.

To get around this, we use a trial-and-error technique, throwing out runs with unfavorable θ and rotating the starting phase angle until a favorable θ is achieved. There is sufficient variation in θ, however, that the outcomes shown in this paper do not always follow a simple pattern, effectively adding to the discreteness noise in the outcome plots (e.g., the B outcome for $q = 1.6\ R_\oplus$, $v_\infty = 4$ km s^{-1}, $P = 10$ h). The overall trends, however, are clear.

3.2.5 Density: Going from the Earth to the Moon

As the Roche limit shows, tidal disruption is a function of the density ratio between the primary target body (planet or moon) and the interloper, albeit one with a weak 1/3 power dependence. Because this parameter has been explored thoroughly by previous groups (e.g., Asphaug and Benz 1996), we have so far restricted ourselves to exploring tidal disruption by the Earth (density 5.5 g cm^{-3}). We now briefly explore the interesting case of tidal disruption by our Moon (3.3 g cm^{-3}). The results for flybys of the Moon by our rubble-pile (P = 6 h, α = 0°) are shown in Fig. 5 (compare with Fig. ??).

It is immediately apparent that the Moon is not nearly as effective as the Earth at disrupting rubble-piles because its Roche sphere is only one quarter the size of Earth's. Hence, for breakup to occur, an asteroid or comet must travel closer to the Moon and have a smaller encounter speed than at the Earth. With the Moon, however, one must also account for an additional factor: the combined attraction of the Earth and Moon. It causes a body with zero velocity at infinity to be accelerated to ~[illegible] km s^{-1} by the time it reaches the Moon. Fig. 5 shows that v_∞ values even slightly in excess of 2 km s^{-1} result in virtually no mass loss. Also note that these results are for favorable values of θ. Hence, though still possible, significant tidal disruption or distortion of ECAs is far more likely to occur in the vicinity of the Earth than the Moon. These results may explain why catena-type crater chains probably do not exist on the Earth (Bottke *et al.* 1997a; *cf.* Section 1.1).

Finally, we note that the lunar results, even though they are somewhat affected by Earth's gravity, suggest that disruption among smaller bodies interacting with one another (i.e., asteroids or comets) is unlikely to occur unless both q and v_∞ are very low.

3.2.6 Shape: Near-spherical progenitor

To gauge how the shape of the rubble-pile affects tidal disruption, we have completed many runs with our code using a near-spherical progenitor. We arranged the particles in "close-hexagonal-packing" form with a packing efficiency of 52%. This yielded a shape of physical dimension 1.93 × 1.92 × 1.88 km. The remaining parameters were similar to the elongated case.

Fig. 9 shows the results for this rubble-pile with P = 6 h and α = 0°. Comparing these results with the elongated progenitor run shown in Fig. ??, we immediately see that our spherical progenitor is much more resistant to tidal disruption, with far fewer instances of S, B, and M class disruptions. Indeed, except at small q, these results are similar to those for an elongated progenitor at the Moon (Fig. 5)! Recall that spherical progenitors have lower gravitational potential energies, making them intrinsically more stable against tidal disruption than other configurations. Thus, spherical bodies, with uniformly small "moment arms", are not subject to as high a degree of tidal stress in close approach as elongated objects with favorable alignment (i.e., θ between 0° and 90°). Note that, for the near-spherical case, the orientation angle θ at perigee has little meaning since the object is nearly symmetric. Otherwise, we see the same trends with respect to q, v_∞, and P as for the elongated progenitor, namely that breakup is favored when these values are small.

We have also examined the effect of the spin axis orientation (α and β) for the near-spherical case. In all runs performed, the results show trends which are consistent with those of the elongated case, although changes in outcome seem less sensitive to variations [illegible]. Hence for the near-spherical case, breakup is still favored for prograde spin (α < 90°) and resisted for retrograde spin (α > 90°).

To check our results, we compare our outcomes to simulations performed by Asphaug and Benz (1996) (their Fig. 14). Like us, they used a spherical rubble-pile with a bulk density of 2.0 g cm^{-3}. However, they used a rubble-pile without rotation on a parabolic trajectory (v_∞ = 0 km s^{-1}), while we used one with P = 6 h prograde on hyperbolic trajectories with $v_\infty \geq 3$ km s^{-1}. Fortunately, from what we have learned in the previous sections, we recognize that the prograde spin in our model is offset to a certain extent by the faster trajectory. Asphaug and Benz found that S-class disruptions occur when $q \lesssim 1.4 R_\oplus$, consistent with our results. Their plot also shows Sridhar and Tremaine's (1992) disruption limit at $q \sim 1.8 R_\oplus$; our results show a B class event at that distance, but N class events further away than that. Thus, the two codes appear to give similar results.

3.2.7 Summary

In general, we find that low values of q, v_∞, and P are needed to cause catastrophic disruptions of rubble-pile ECAs. Retrograde rotation, on the other hand, dramatically reduces the severity of disruptions for a given set of q, v_∞, and P, as does an unfavorable orientation at perigee. Hence among actual randomly oriented and spinning objects encountering the Earth, only half are likely to have their long axis orientated at perigee such that a disruption event is likely. Of the rest, roughly half with low P encounter the Earth with favorable rotation; more leeway is allowed for objects with high P. Thus, we estimate that elongated rubble-piles with low q, v_∞, and P have roughly a 25% chance of undergoing a tidal disruption event each time they encounter the Earth. These odds can increase up to ~ 50% if the object has a large P, though q and v_∞ must be correspondingly lower.

3.3 Discussion

As we have shown, tidal disruption ejects clumps and fragments of many sizes from our progenitor, often leaving the remnant with an unusual shape and a new rotation period. Table I provides data for more quantitative analysis of the generic $P = 6$ h Earth encounter (Fig. ??). Similar tables are available for the other runs discussed in this paper, on request to the authors. In the Table, q, v_∞, and θ have the usual definitions; "C" is the outcome class; $P_{\rm rem}$, $\varepsilon_{\rm rem}$, and $M_{\rm rem}$ are as defined in Section 2.4.2; $M_{\rm acc}$, $M_{\rm orb}$, and $M_{\rm esc}$ are the mass fraction of material accreting, orbiting, and escaping the remnant, respectively (Section 2.4.3; note $M_{\rm rem} + M_{\rm acc} + M_{\rm orb} + M_{\rm esc} \equiv 1$); and δR is a clump size distribution statistic, defined below. A dagger (†) in the Notes column indicates runs with $\theta < 25°$ or $\theta > 65°$. These runs should not be considered representative of the maximum disruption state for that choice of parameters due to the marginal θ values.

3.3.1 Ejecta statistics

For the S class outcomes, the average $M_{\rm acc}/M_{\rm orb}/M_{\rm esc}$ values are 0.008/0.075/0.629, respectively, while the mean remnant mass fraction, $\bar{M}_{\rm rem}$, is 0.288. Approximately 10.4 clumps on average are created in each of these events, with each clump accounting for $\sim 6.0\%$ of the mass of the original progenitor (i.e., a fractional mass of 0.06 each). The statistics for all 74 S class events seen in Fig. 4 taken as a whole were similar: mean ejecta fractional masses of 0.023/0.048/0.681, $\bar{M}_{\rm rem} = 0.247$, and 10.8 clumps created per event, with an average mass fraction of 0.062 each. Individual particles were also stripped away, but they were found to comprise less than 1% of the progenitor's mass.

The size distribution of the S class clumps is difficult to determine reliably without using more particles to increase the resolution. A crude quantitative measure is given in Table I by δR, the ratio of the standard deviation of the sizes of all clumps in the outcome to the size of the largest remnant. Values of δR near zero imply uniformity (values of exactly zero generally mean no clumps were stripped from the progenitor; for these cases the entry under δR is blank). Our results show that S class events cover a wide range of δR values but generally have $\delta R < 0.5$. For example, the first run listed in the Table produced 18 similarly-sized clumps, yielding a δR value of 0.18. Two other less energetic disruptions (with larger q but same v_∞) generated fewer, less uniform clumps, yielding δR values of 0.47 (*cf.* Fig. 6, though the differences are difficult to discern by eye).

The B class outcomes in Table I yield similar mean $M_{\rm acc}$ and $M_{\rm orb}$ ratios to those of S class outcomes, but far smaller mean $M_{\rm esc}$ values: 0.052/0.064/0.084, with $\bar{M}_{\rm rem} = 0.799$. Here, only 2.5 clumps on average are created per event, each with an average mass fraction of 0.072. Thus, fewer clumps are shed, but the clumps themselves are roughly the same size as those formed in S class events. For the 43 B class events found in Fig. 4 taken as a whole, the results are again similar: ejecta mass fractions 0.039/0.064/0.126, $\bar{M}_{\rm rem} = 0.771$, 3.3 clumps of fractional mass 0.064 each created per event. The remaining ejecta is predominantly individual particles; roughly four are shed during each event. They still constitute only a small mass fraction. The average δR value for the B class events shown in Table I is 0.59, larger than for any S class event. This increase indicates that B class ejecta is less uniform than the S class clumps seen previously.

Marginal S class/B class disruptions often produce two or three big components which are close to one another. An example of this would be the two B class outcomes in the table with low δR values; Fig. 6 indicates they are practically fission events. Comparable fission events are observed when the spin axis or long axis orientation angles differ from their nominal values ($\alpha = 0°$; $\theta \sim 45°$) in what would otherwise be a typical S class disruption. Though we have not yet completed enough runs to do a quantitative study, we hypothesize that some of the contact-binary shapes seen among the Earth-crossing asteroids (e.g., 4769 Castalia, 2063 Bacchus) may have been produced by these fission-type events (Section 4.1).

Mild M class disruptions, by definition, eject little material. For this reason, the results for these cases must be interpreted with caution, since the resolution of our rubble-pile was probably too coarse to detect marginal mass loss or clump formation. The ejecta mass fractions for the M class disruptions in Table I are 0.000/0.014/0.018, with $\bar{M}_{\rm rem} = 0.968$. A single clump containing 3 or 4 particles was created 63% of the time (5 cases out of 8). Results for all 56 M class events in Fig. 4 followed a similar trend: 0.006/0.014/0.017, $\bar{M}_{\rm rem} = 0.963$, 1.05 clumps ejected 43% of the time, with mass fractions of 0.013. Ejected single particles (or groups of two particles) were found to be relatively more important in these mild disruption cases. M class events shed, on average, 4 un-clumped particles per event, though this range can vary widely. In one case reported in Table I, the progenitor expelled 10 particles, while in a second case, only a single particle was lost. For these cases, δR is not a particularly meaningful statistic, but the average value for the clump-shedding M class outcomes shown in Table I clumps is 0.93.

In summary, we find two broad types of ejecta size distributions: (1) an SL9-type distribution of several similar-sized fragments and scattered smaller fragments; and (2) mass shedding events producing small clumps and fragments

3.3.2 Orbital parameters of 1)01111(1 ejecta

Although the bulk of all shed material ultimately escapes the remnant rubble-pile, a nonetheless significant amount remains in orbit around the progenitor (22% of all the material averaged over all disruptive outcomes). Thus, it is likely that tidal disruption is capable of creating binary asteroids (Bottke and Melosh 1996a, b; *cf.* Section .1.1).

At least 23 of the 27 S, B, and M class events in Table I place clumps or single particles into bound orbits. This value might be even higher, since we only consider bound orbits around the remnant rubble-pile; S class events may create multiple binary systems. On average, each disruption places two fragments (clumps or single particles) into orbit.

The median semimajor axis among all 47 orbiting fragments found in the Table I runs is 6.2 km. The mean is much higher (56 km, with standard deviation $\sigma = 249$ km) since four fragments were thrown 0111 to $a = 138$–1680 km. The median eccentricity for the 47 bodies is 0.77, with the mean slightly smaller (0.73, $\sigma = 0.20$). The median periapse (2.0 km) is small enough that a number of these orbits are probably unstable.

Finally, the median inclination of these bodies is 7.2°, with the average slightly higher (12.3°, $\sigma = 18.3°$). These low values are not surprising, given that most particles are stripped off in the rubble-pile's equatorial??? plane as tidal torques produce an excess of rotational angular momentum. Future searches for binaries among ECAs should probably be directed toward the equatorial??? plane of the body.

3.3.3 Spin and shape changes

The $P_{\rm rem}$ and $\varepsilon_{\rm rem}$ columns of Table I show the effect of tidal disruption on progenitor spin and shape. In each case the remnant is stable against rotational disruption, as defined by Eq. (1) (where we have taken $a/b = 1/(1 - \varepsilon_{\rm rem})$ by invoking the approximation $b = \frac{1}{2}(a_2 + a_3)$, i.e., b is taken to be the mean minor axis and $a \equiv a_1$, and we have assumed the bulk density of the remnant remains largely unchanged). For example, a body with a density of 2 g cm^{-3} and $P = 3.5, 4.0, 4.5, 5.0, 5.5$, and 6.0 h sheds mass when $\varepsilon_{\rm rem} = 0.56$, 0.66, 0.73, 0.78, 0.82, and 0.85. Thus none of the remnants in Table I are in danger of flying apart from rotation alone. Note that our elongated progenitor rubble-pile, with $\varepsilon_{\rm rem} = 0.43$, is also stable for the spin periods tested. Our nearly spherical rubble-pile, with $\varepsilon_{\rm rem} = 0.02$, is rotationally stable for all $P \gtrsim 2.3$ h.

We find that most S and some B class events are so destructive that the spin and ellipticity of the remnant are only mildly correlated with the progenitor values. For S class events, gravitational instabilities cause particles to agglomerate after the disruption, leaving behind near-spherical clumps whose final spins are determined by conservation of angular momentum. For B class events, large clumps stripped away from the rubble-pile may also leave behind more spherical remnants.

Many B and M class events, however, can cause substantial $\varepsilon_{\rm rem}$ increases since tidal forces are only strong enough to elongate the progenitor and strip small amounts of mass from the ends. The most extreme example in the Table (also see Fig. 6) has $\varepsilon_{\rm rem} = 0.65$ for the M class $q = 1.4\ R_\oplus$, $v_\infty = 18$ km s^{-1} encounter. Eccentricities as high as 0.69 have been noted in other runs as well. The spin rate only increases by a small amount, though, as tidal torquing and conservation of angular momentum compete.

Finally, as the outcomes become even less destructive (weak M and non-disruptive N class), the values of $\varepsilon_{\rm rem}$ only marginally increase. Spin rates, on the other hand, can still increase considerably, even for large q encounters. For example, the N class event for $q = 3.8\ R_\oplus$, $v_\infty = 12$ km s^{-1} shows a decrease in P from 6 to 4.5 h. If succeeding encounters were prograde, therefore, the object would be much more likely to disrupt.

Another observation (not shown in the Table) is that retrograde encounters generally reduce the rubble-pile's ellipticity, sometimes to near zero (values as low as 0.07 were noted for some $P = -12$ h cases). In these cases the rotational inertia opposes the tidal stretching of the body, causing the rubble-pile to collapse (*cf.* Section 3.2.4). The final rotation period $P_{\rm rem}$ depends on the size of the torque relative to the magnitude of rotational inertia in the system. For example, a $P = -12$ h test body that experienced strong torque ($q = 1.4\ R_\oplus$ and $v_\infty = 12$ km s^{-1}) had its spin reversed ($P_{\rm rem} = +10.3$ h) and had its elongation strongly reduced ($\varepsilon_{\rm rem} = 0.11$). On the other hand, a test body subjected to weak torque ($P = -12$ h, $q = 2.2\ R_\oplus$, and $v_\infty = 12$ km s^{-1}) experienced far less change in spin and ellipticity ($P_{\rm rem} = -10.5$ h, $\varepsilon_{\rm rem} = 0.35$). In this case the slight increase in retrograde spin correlates well with the mild contraction of the body, indicating that rotational inertia and conservation of angular momentum dominated over the tidal torque.

Shape and spin changes are similarly dependent on the orientation of the phase angle θ, with angles between 0° and 90° providing maximum torque (Section 3.2.4). This result holds even for retrograde encounters: one run with $q = 1.4\ R_\oplus$, $v_\infty = 6$ km s^{-1}, $P = -6$ h, and $\theta = 58°$ had P increase to $+5.4$ h, while a second run with the same orbital parameters and $\theta = 141°$ had P increase from -6 to $+6.9$ h. In both cases, the rubble-pile ended up being nearly spherical.

3.3.4 Long term evolution

The evolution of the rubble-pile and any shed fragments is not necessarily completed by the end of the simulation. Recall that $M_{\rm rem}$ alone defines the outcome class (Section 3.1); we do not add the mass fraction $M_{\rm acc}$ to $M_{\rm rem}$, even though it could potentially change the outcome class. This is unlikely for most of the runs in Fig. 4, however, since most ejecta are on escape trajectories. Nevertheless, as a check we integrated a few representative cases over ten times the initial time interval. To control the secular increase in angular momentum, we reduced our time-step criterion significantly, which in turn drastically increased the computation time. Our results indicate no outcome class changes, but some minor changes to the remnant rubble-pile properties do occur as material is reagglomerated. Further work needs to be done to study the long term evolution of these models.

4 CONCLUSIONS

4.1 Applications

Starting from the premise that Earth-crossing asteroids are intrinsically weak rubble-piles, our simulations provide explanations for some unusual phenomena in the terrestrial planet region. The implication of this work is that planetary tidal forces play a much larger role in the evolution of near-Earth asteroids than previously thought

4.1.1 Tidal disruption rates near the Earth

To gauge the effectiveness and importance of tidal disruption in the terrestrial planet region, we can estimate the frequency of S, B, and M class events near the Earth. We already have a map of tidal disruption outcomes as a function of P, q, v_∞, α, β, and θ (Section 3). We also require estimates of the following quantities: (a) encounter probability of ECAs with Earth; (b) probability distribution of ECA encounter velocities with the Earth; (c) probability distribution of rotation periods among ECAs; and (d) size-frequency distribution of (rubble-pile) asteroids in the ECA population. These components and the method for incorporating them into the calculation are described in Bottke *et al.* (1997a). This earlier work however did not include the $P = -12$ h and $P = \infty$ runs, which we incorporate here. Given that retrograde rubble-piles become succeedingly more difficult to disrupt as their spin rate increases, and that no mass loss is seen for $P = 6$ h, we assume that tidal disruption terminates at $P \sim 9$ h. CHECK THIS???

Our results indicate that the lifetime of rubble-pile ECAs against S class events is 380 Myr, the lifetime against S or B class events is 220 Myr, and the lifetime against S, B, or M class events is 86 Myr. Applying this lifetime to the estimated number of km-sized ECAs (2100; Morrison 1992), we find that S class events occur near the Earth once every 183,000 yr, S and B events once every 104,000 yr, and S, B, and M events once every 41,000 yr. Note that these rates would increase if we included Venus crossings, since our sister planet is nearly as effective as the Earth at tidal disruption.

Bottke *et al.* (1998???) used these results SHOULD WE UPDATE??? to estimate the total mass shed by ECAs over time. They found that roughly 6×10^7 kg per year are lost, equivalent to the annual injection rate of 50 m fragments into the 3:1 or ν_6 resonances (Menichella *et al.* 1996). CONSISTENCY PROBLEM: 50 m RESOLUTION???

4.1.2 Crater chain formation on the Earth and Moon

As described in Section 1, some catena-type crater chains are thought to be formed via S class disruption of rubble-pile asteroids or comets. In this scenario, the fragment train hits a moon of the planet soon after the disruption event, before the train has stretched so far that it can no longer produce a recognizable crater chain on impact. Chains formed by this mechanism can be discriminated from those produced by secondary ejecta, since the latter can be identified by their radial orientation to the source crater their association with other secondary features, and their distinctive morphology (e.g., "herringbone" patterns). Note that studies have shown that rubble-pile clumps, despite being intrinsically weak objects, can nonetheless produce well-defined craters on impact (e. g., Schultz and Gault 1985; Melosh 1989; Love *et al.* 1995).

Nearly twenty crater chains have been identified on Ganymede and Callisto, ranging between 60 626 km in length and featuring 6 25 closely similar-sized craters (Schenk *et al.* 1996). One or two analogous crater chains have been identified on Earth's Moon (Melosh and Whitaker 1994; Wichman and Wood 1995; Schenk *et al.* 1996). They include the Davy which is 47 km long and contains 23 craters, each 1 3 km in diameter, and the Abulfeda chain, which is $\gtrsim 3.8$ Gyr old, 200 260 km long and has 24 craters, each 5 13 km in diameter. There have even been reports of one or two crater chains on the Earth. One such proposed chain is a 700 km line of eight circular depressions crossing Kansas, Missouri, and Illinois (Rampino and Volk 1996). Each depression is 3 17 km wide. A second potential chain is located in Chad, where two possible impact features discovered by radar lie near the 17 km diameter, 360 Myr old Aorounga impact structure (Ocampo and Pope 1996). Both of these claims are controversial and need to be verified by field work.

Using an earlier set of the runs presented here, Bottke *et al.* (1997a) examined whether km-sized ECAs undergoing S class events near the Earth or Moon could make lunar or terrestrial crater chains. They found that enough objects have undergone S class events near the Earth over the last 3.8 Gyr to account for 1 crater chain on the Moon, consistent with observations. Given that the Moon is a small target far from Earth, this match suggests that tidal disruption near Earth may be common.

The number of chains expected to be formed on the Earth over the same time, however, was found to be less than 0.1 Moreover, the number expected on Earth over the last 360 Myr was only 0.001, inconsistent with the proposed terrestrial crater chains. Some uncertainty in the calculation can be eliminated by taking the ratio of the production rate of crater chains on the Moon to that on Earth (see Appendix B for a semi-analytic derivation of this ratio). Bottke *et al.* (1997a) found that the lunar production rate is ~ 10 times the terrestrial rate. Thus, if there are one or two crater chains on the Earth less than 360 Myr old, roughly 10–20 young, fresh crater chains should be found on the Moon's near side. No such chains have been observed. Bottke *et al.* (1997a) concluded that the reported terrestrial crater chains, if real, were not produced by lunar tidal forces.

4.1.3 Formation of binary asteroids and doublet craters

At least 3 of the 28 largest known impact craters on Earth and a similar fraction of all impact structures on Venus are doublets, formed by the nearly simultaneous impact of objects of comparable size (Bottke and Melosh 1996a,b). Mars also has doublet craters, though the fraction found there is smaller (2–3%) (Melosh *et al.* 1996). These craters are too large and too far separated to have been formed by tidal disruption just before impact or from asteroid fragments dispersed by aerodynamic forces during entry. Based on this, Melosh and Stansberry (1991) concluded they had to have been formed from a population of binary asteroids.

As mentioned in Section 1, Bottke and Melosh (1996a,b) found that the components of contact binaries can be pulled apart but remain gravitationally bound to one another, evolving into a stable binary system. They hypothesized that more complicated systems with several satellites (i.e., from tidally disrupted rubble-piles) would evolve like a multiple star system, with the most stable endstate being a binary system. Such a binary system could re-encounter and hit a planet during a later pass, creating two distinct craters (note that this explains why triplet or even quadruplet craters are not seen, since the corresponding orbital systems are intrinsically unstable). Their numerical results suggest that $\sim 15\%$ of all Earth-crossing asteroids (and $< 5\%$ of solely Mars-crossers) evolve into co-orbiting binary asteroids with well-separated components. Folding these results into another model treating impact encounters between binary asteroids and a given planet, they found they could duplicate the observed fraction of doublet craters found on Earth, Venus, and Mars.

Our results, using a more sophisticated code and rubble-pile progenitor, verify these ideas. Our runs indicate that at least 76% of all our S, B, and M class events produce fragments which were at least initially gravitationally bound to the remnant progenitor. As before, this value could be much higher, since, for S class events, we only consider bound orbits around the largest aggregate. In general, the bound fragments were small clumps or individual particles. Some S class events, however, show clumps of nearly equal size moving in orbit around one another. These types of events may be responsible for doublet craters with nearly equal size components (e.g., East and West Clearwater Lake in Canada). The dynamical lifetime of ECAs against planetary collision, catastrophic collision with another asteroid, or ejection by Jupiter perturbations is thought to be on the order of 10 Myr (Milani *et al.* 1989; Michel *et al.* 1996; Gladman *et al.* 1997). Since our previous calculation showed that a rubble-pile's lifetime against S, B, and M events is 86 Myr, we predict that $\sim 10\%$ of the ECA population are binary asteroids, almost exactly the value found by Bottke and Melosh (1996a,b).

4.1.4 ECAs with satellites: An examination of 3671 Dionysus

Pravec *et al.* (1996) and Mottola and Hahn (1997) claim to have discovered satellites orbiting Earth-crossing asteroids 1994 AW$_1$ and 3671 Dionysus, respectively. These claims are based on periodic dips in each asteroid's lightcurve, interpreted as stemming from eclipses due to orbiting companions. In the case of Dionysus, however, future eclipse events were both predicted and then confirmed by other observers, mitigating the possibility they were produced by anomalous features in the lightcurve.

Since both objects have parameters which make them likely candidates for tidal disruption, we believe this mechanism created the alleged satellites. For example, 3671 Dionysus is slightly elongated (1.3×1.0 km; S. Hahn, personal communication) and has orbital parameters of $a = 2.19$ AU, $e = 0.51$; $i = 13.6°$. Using the method of Bottke *et al.* (1994a,b) we calculated its intrinsic collision probability P_i with Earth (40.5×10^{-18} km^{-2} yr^{-1}) and its average v_∞ (10.91 km s^{-1}). Neither value is exceptional: the collisional lifetime of Dionysus with Earth (295 Myr) is nearly twice as long as the mean of the ECA population, while its v_∞ is only slightly below the mean (Bottke *et al.* 1994b). The spin rate of Dionysus, however, is so fast ($P = 2.7$ h) that the object is close to the rotational break-up limit given by Eq. (1). We have not performed any runs with $P = 2.7$ h, but as an approximation we can apply our $P = 4$ h results to the problem. Assuming from Fig. 4 that tidal disruption occurs if Dionysus passes within $\sim 5\ R_\oplus$ of Earth at $v_\infty = 9$ km s^{-1}, and that its nearly spherical shape means we can neglect the effect of θ, we estimate that its lifetime against tidal disruption is between 20–40 Myr, almost 7.5–15 times smaller than its collision lifetime. Given the range of possible outcomes seen in our results, there is a distinct possibility that this object's satellite, its fast rotation rate, and its nearly spherical shape may be a by-product of tidal disruption.

We recommend that observers searching for binaries among the ECAs look for the following parameters: (1) low encounter velocities with Earth or Venus; (2) high P_i values; (3) fast rotation rates; and (4) elongated shapes. Note that (1) and (2) are produced when ECAs have low i values and/or when they have perigees (q) or apogees (Q) near 1 AU.

4.1.5 ECAs with irregular shapes: An examination of 1620 Geographos and double-lobed bodies

RADAR PIC OF GEOGRAPHOS?

Over the past several years, Steve Ostro and his associates have used delay-Doppler radar techniques to determine the shapes of several ECAs (Ostro 1993) A large fraction of this set have unusual shapes which we believe are consistent with reshaping by planetary tides.

For example, 1620 Geographos (a = 1.25 AU, e = 0.336, i = 13.3°) is one of the most elongated objects known in the solar system (5.11 × 1.85 km; Ostro *et al.* 1995a). Solem and Hills (1996) were the first to suggest that Geographos could have been reshaped by tides. We have followed up on their work by increasing the resolution, including the effects of rotation, and by examining a larger set of encounter parameters. Assuming the minor axes have roughly the same dimension, we estimate that Geographos has an ellipticity of $\epsilon_{\rm rem}$ = 0.64. We note Geographos's radar silhouette indicates that one end is tapered much like a jalapeño. There are also cusps on the ends which are swept back against the rotation direction, giving the body the appearance of a "pinwheel" when viewed from various aspect angles (Ostro *et al.* 1996). Finally, the rotation period of Geographos is short (5.22 h), such that the ends are not far from rotational break-up.

These features are diagnostic of a body that has undergone B or M class disruption, particularly like those listed in Table 1 for which $\epsilon_{\rm rem} > 0.60$ (also see Fig. ??). In each case, the end closest to Earth at perigee loses the most mass, leaving it distinctly stretched and tapered compared to the opposite end. The observed cusps are remnants of Keplerian shear among the ejected fragments. We found that 27 of the 117 B and M class outcomes displayed in Fig. 4 and Fig. 8 (~ 23%) have $\epsilon_{\rm rem} \geq 0.60$, suggesting these shapes are common. The median rotation period for these 27 events was 5.22 h, exactly the same as Geographos. Thus, we find it likely that Geographos is a tidally distorted object (Bottke *et al.* 1997b???).

Three of the ECAs imaged so far by delay-Doppler radar techniques, 4769 Castalia, 2063 Bacchus, and 4179 Toutatis, have double-lobed shapes. It is possible that some of these objects may be contact binaries. If so, they may have been influenced or even created by planetary tidal forces.

4769 Castalia has dimensions of 0.7 × 1.0 × 1.6 km, giving it an ellipticity of $\epsilon_{\rm rem}$ = 0.47 (Hudson and Ostro 1995a). Its fast rotation rate (P = 4 h) and favorable orbital parameters (a = 1.06 AU, e = 0.48, i = 8.9°, allowing it to cross both the orbits of Earth and of Venus with $v_\infty \sim 16$ km s^{-1}), make it a good candidate for tidal disruption.

2063 Bacchus, an ECA on a Castalia-like orbit (a = 1.08 AU, e = 0.35, i = 9.4°), can encounter Earth and Venus at even lower v_∞ (~ 10–11 km s^{-1}). Its rotation period, however, is much longer (nearly 15 h; Benner *et al.* 1997).

4179 Toutatis (a = 2.52 AU, e = 0.635, i = 0.472°) is an ECA with dimensions of 1.92 × 2.40 × 4.60 km ($\epsilon_{\rm rem}$ = 0.53). It also has a tumbling rotation state which gives it a period of 130 h (Hudson and Ostro 1995b). Its very low inclination, however, makes it five times more likely to encounter the Earth at $v_\infty \sim 12$ km s^{-1} than a typical ECA.

Our results indicate that contact binaries may be produced by weak S or strong B class events, where large similar-sized components typically near the center of the fragment train often crash into one another at such gentle speeds and with sufficient rotation that the new aggregate retains a double-lobed shape. For example, the P = 6 h, $q = 1.8\ R_\oplus$, v_∞ = 6 km s^{-1} outcome shown in Fig. 6 produces such a contact binary (see Fig. ??a for a close-up view). The run with P = 10 h, $q = 1.6\ R_\oplus$ and v_∞ = 8 km s^{-1} does as well (Fig. ??b). NEED SOME STATS HERE???

4.1.6 Size and orbital distribution of ECAs: Evidence for tidal disruption?

Tidal disruption, occurring at low v_∞, may produce enough small bodies to enhance the local population. A qualitative check by Bottke *et al.* (1998???) of the size and orbital distribution of the known ECA population shows few large bodies but many small bodies with low e, i. These features may be consistent with tidal disruption, though we cannot say how much the known ECA population suffers from observational selection effects (see Jedicke 1996 for more information). These results may also explain the population of small

Earth-crossing objects suggested by Spacewatch (Rabinowitz *et al.* 1993; Rabinowitz 1994; Bottke *et al.* 1998???), a possibility also suggested by Asphaug and Benz (1996) and Solem and Hills (1996).

4.2 Future Work

In this paper, we have explored many of the parameters important for tidal disruption: trajectory (q, v_∞), rotation (P), spin axis orientation (α, β), shape, long axis phase angle (θ), and density. Practical considerations prevented systematic exploration of these variables over all possible ranges that lead to tidal disruption, but we feel we have obtained a good parameterization of the basic encounter outcomes. Higher resolution sampling in the q-v_∞-P space is desirable, but unlikely to yield much in the way of new results. A more thorough investigation of progenitor shape effects is probably of greater importance, along with a better understanding of the role of α, β, and θ. As computer power and availability improve, we plan to explore these issues in greater detail.

We also intend to explore the internal structure of the rubble-pile itself. Although more sophisticated than previous studies, our model is nonetheless crude. One refinement would be to increase the resolution by including more particles, but this would require considerably more computation time. A few representative cases may allow us to estimate the importance of higher resolution (we have done this to a certain extent till'(ii(1)". and found that higher resolution smooths out the boundary between M and N class disruption). A second refinement would be to examine rubble-piles with a non-uniform particle size distribution. Clump formation may be enhanced by the use of a size distribution since the larger particles become natural seeds for agglomeration of the smaller ones (Richardson *et al.* 1995). Smaller particles filling the gaps between larger particles could also provide higher bulk densities in the same volume. It would also be interesting to consider the effects of using more realistic non-spherical constituent particles. Interlocking between such particles could lead to even larger potential energy barriers allowing the formation of irregular shaped rubble-piles. However this is much harder to implement numerically than simple spheres. More readily testable is the inclusion of SIIP' fil(,(friction between the spheres, although preliminary investigation of this effect shows that it manifests itself only as a slightly increased damping without changing the outcome very much (Richardson *et al.* 1995).

Finally, with the data already in hand, it may be possible to develop an analytical theory to predict tidal disruption outcomes on the basis of the parameters explored here. Some steps toward this end have been taken already (*cf.* Section 3), but much remains to be done.

It is our belief that tidal disruption and studies of rubble-piles in general will continue to be a fruitful line of research in the field of planetary science. Ultimately such research may contribute to a unified model of small bodies in the solar system that ('01111)111(,> both orbital and physical evolution.

A Derivation of Encounter Time

For a hyperbolic trajectory, the time since close approach is given by Goldstein (1980):

$$t = \sqrt{\frac{a^3}{GM_\oplus}} \int_0^{F} (e \cosh F' - 1)\, dF', \tag{12}$$

where a is the semi-major axis of the orbit, e is the orbital eccentricity ($e > 1$), and F is the hyperbolic analogue of the eccentric anomaly defined by:

$$r = a(e \cosh F - 1), \tag{13}$$

where r is the distance from the central mass, in our case the Earth. The orbital parameters can be obtained from (Goldstein 1980):

$$\frac{1}{a} = \frac{v^2}{GM_\oplus} - \frac{2}{r}, \tag{14}$$

where v is the orbital speed with respect to the Earth, and

$$q = a(e - 1). \tag{15}$$

Eq. (14) can be written in terms of v_∞ by setting $r \to \infty$:

$$\frac{1}{a} = \frac{v_\infty^2}{GM_\oplus}. \tag{16}$$

Hence if the initial distance (15 $R_{\rm Roche}$) is r_i and the final distance (60 $R_\oplus$) is r_f, then the total encounter time is given by:

$$T = \sqrt{\frac{a^3}{GM_\oplus}} \left[e(\sinh F_i + \sinh F_f) - (F_i + F_f)\right], \tag{17}$$

where

$$F_i = \cosh^{-1}\left[\frac{1}{e}\left(1 + \frac{r_i}{a}\right)\right], \tag{18}$$

$$F_f = \cosh^{-1}\left[\frac{1}{e}\left(1 + \frac{r_f}{a}\right)\right], \tag{19}$$

and

$$a = \frac{GM_\oplus}{v_\infty^2}, \quad e = \frac{q}{a} + 1. \tag{20}$$

For example, the S class run shown in Fig. 2a had a total encounter time of 30.1 h, of which 1.3 h was spent within the Roche limit (3.4 $R_\oplus$). By contrast, the N class run in Fig. 2d had an encounter time of 21.1 h and spent only 34 min at the edge of the tidal limit.

B Crater Chains on the Earth and Moon: Semi-analytical Derivation

The number of ECAs larger than a given diameter D that pass a distance r from the center of Earth without striking the Earth is given by:

$$F_{\rm Earth} = P_i N_D \left\{ r^2 \left[1 + \frac{v^2_{{\rm esc},\oplus}(r)}{v_\infty^2}\right] - R_\oplus^2 \left[1 + \frac{v^2_{{\rm esc},\oplus}(R_\oplus)}{v_\infty^2}\right]\right\}, \tag{21}$$

where

$$v_{{\rm esc},\oplus}(r) = \sqrt{\frac{2GM_\oplus}{r}} \tag{22}$$

is the escape speed from the Earth a distance r from its center, $R_\oplus$ and $M_\oplus$ are the radius and mass of the Earth, respectively, v_∞ is the speed of the asteroid before the gravitational acceleration of the Earth is included, P_i is the intrinsic collision probability of ECAs with the Earth (Bottke *et al.* 1994a,b), and N_D

is the cumulative number of ECAs larger than D. The number of bodies that pass through this annulus to strike the Moon is:

$$F_{\mathrm{Moon\ Impact}} = F_{\mathrm{Earth}} \left(\frac{\pi R_{\mathrm{M}}^2}{4\pi d^2}\right) \left[1 + \frac{v_{\mathrm{esc,M}}^2(R_{\mathrm{M}})}{v_\infty^2 + v_{\mathrm{esc},\oplus}^2(d)}\right], \tag{23}$$

where

$$v_{\mathrm{esc,M}}(r) = \sqrt{\frac{2GM_{\mathrm{M}}}{r}} \tag{24}$$

is the escape speed from the Moon a distance r from its center, R_{M} and M_{M} are the radius and mass of the Moon, respectively, and d is the Moon's distance from the Earth.

To estimate the flux of crater chains formed on the Moon over time, we define the parameter $r_{\mathrm{S},\oplus}$, the *minimum* Earth approach distance needed for an asteroid to undergo an S class event:

$$r_{\mathrm{S},\oplus} = f_{\mathrm{S},\oplus} R_\oplus \tag{25}$$

where $f_{\mathrm{S},\oplus}$ is a dimensionless factor that depends on quantities such as the progenitor's encounter speed, its spin period, its bulk density, etc. Note that $r_{\mathrm{S},\oplus}$ can currently only be found numerically, but that the final result is *comparable to the* Earth's Roche radius. The escape speed at $r_{\mathrm{S},\oplus}$ is then given by:

$$v_{\mathrm{esc},\oplus}(r_{\mathrm{S},\oplus}) = \sqrt{\frac{2GM_\oplus}{r_{\mathrm{S},\oplus}}} = f_{\mathrm{S},\oplus}^{-1/2}\, v_{\mathrm{esc},\oplus}(R_\oplus), \tag{26}$$

allowing us to rewrite Eq. (21) as:

$$F_{\mathrm{Earth}} = P_i N_D R_\oplus^2 \left[(f_{\mathrm{S},\oplus}^2 - 1) + (f_{\mathrm{S},\oplus} - 1)\frac{v_{\mathrm{esc},\oplus}^2(R_\oplus)}{v_\infty^2}\right] \tag{27}$$

We now perform the analogous steps for objects disrupted by the Moon. The number of ECAs larger than a given diameter D that pass within a distance r from the Moon without striking it is given by:

$$F_{\mathrm{Moon}} = P_i N_D \left\{ r_{\mathrm{M}}^2 \left[1 + \frac{v_{\mathrm{esc,M}}^2(r)}{v_\infty^2 + v_{\mathrm{esc},\oplus}^2(d)}\right] - R_{\mathrm{M}}^2 \left[1 + \frac{v_{\mathrm{esc,M}}^2(R_{\mathrm{M}})}{v_\infty^2 + v_{\mathrm{esc},\oplus}^2(d)}\right]\right\} \tag{28}$$

where we have accounted for the acceleration of the objects due to the Earth. The number of bodies undergoing S class events (a distance $r_{\mathrm{S,M}}$ from the Moon) is therefore:

$$F_{\mathrm{Moon}} = P_i N_D R_{\mathrm{M}}^2 \left[(f_{\mathrm{S,M}}^2 - 1) + (f_{\mathrm{S,M}} - 1)\frac{v_{\mathrm{esc,M}}^2(R_{\mathrm{M}})}{v_\infty^2 + v_{\mathrm{esc},\oplus}^2(d)}\right] \tag{29}$$

where $f_{\mathrm{S,M}}$ is the equivalent of $f_{\mathrm{S},\oplus}$ for the Moon. Finally, the number of bodies that disrupt near the Moon and go on to hit the Earth is given by:

$$F_{\mathrm{Earth\ Impact}} = F_{\mathrm{Moon}} \left(\frac{\pi R_\oplus^2}{4\pi d^2}\right) \left[1 + \frac{v_{\mathrm{esc},\oplus}^2(R_\oplus)}{v_\infty^2}\right] \tag{30}$$

Taking the ratio of the flux of crater chains formed *on the Moon* ($F_{\mathrm{Moon\ Impact}}$) to that of the Earth ($F_{\mathrm{Earth\ Impact}}$), we find that many parameters drop out of the equation, leaving

$$\frac{F_{\mathrm{Moon\ Impact}}}{F_{\mathrm{Earth\ Impact}}} = \frac{\left[(f_{\mathrm{S},\oplus}^2 - 1) + (f_{\mathrm{S},\oplus} - 1)\left(\frac{v_{\mathrm{esc},\oplus}^2(R_\oplus)}{v_\infty^2}\right)\right]\left[1 + \frac{v_{\mathrm{esc,M}}^2(R_{\mathrm{M}})}{v_\infty^2 + v_{\mathrm{esc},\oplus}^2(d)}\right]}{\left[(f_{\mathrm{S,M}}^2 - 1) + (f_{\mathrm{S,M}} - 1)\left(\frac{v_{\mathrm{esc,M}}^2(R_{\mathrm{M}})}{v_\infty^2 + v_{\mathrm{esc},\oplus}^2(d)}\right)\right]\left[1 + \frac{v_{\mathrm{esc},\oplus}^2(R_\oplus)}{v_\infty^2}\right]} \tag{31}$$

The *remaining* variables, $f_{\mathrm{S,M}}$, $f_{\mathrm{S},\oplus}$, and v_∞ can be estimated from Fig. ?? and Fig. 5. For rubble-piles with rotation periods of 6 h, $f_{\mathrm{S,M}} \sim 1.1$ for $v_\infty = 3$ km s^{-1}, while $f_{\mathrm{S},\oplus} = 2.2, 1.4, 1.4$ for $v_\infty = 3, 6, 9$ km s^{-1}, respectively. *Other values are assumed* to be *negligible* for this appoximation. Substituting and taking the ratio, we find that about nine crater chains are made on the Moon for every one that is made on the Earth. Using more exact measurements, Bottke *et al.* (1997a) *found this ratio* was ~ 10, a very good match. Since only one or two crater chains have been formed on the Moon over the last 3.8 Gyr, it seems unlikely that any crater chains have been formed on the Earth within the last few *hundred million years.*

Acknowledgments

This research was supported by Derek Richardson's Natural Sciences and Engineering Research Council (NSERC) Fellowship at the Canadian Institute for Theoretical Astrophysics (CITA) and a NASA HPCC/ESS grant NAG 5-2213 held at the University of Washington, William Bottke's Texaco Prize Fellowship at Caltech, and Stanley Love's O.K. Earl Prize Fellowship at Caltech.

The authors would like to thank Erik Asphaug, Lance Benner, Joe Burns, Paolo Farinella, Alan Harris, Jay Melosh, Patrick Michel, Paul Weissman, and MORE??? for their valued contributions to this project.

References

Aarseth, S. J. 1985. Direct methods for *N*-body simulations. In *Multiple Time Scales* (J. U. Brackill and B. I. Cohen, Eds.), pp. 377–418. Academic Press, New York.

Aggarwal, H. R., and V. R. Oberbeck 1974. Roche limit of a solid body. *Astrophys. J.* **191**, 577–588.

Asphaug, E., and W. Benz 1994. Density of comet Shoemaker-Levy 9 deduced by modelling breakup of the parent "rubble pile". *Nature* **370**, 120–124.

Asphaug, E., and W. Benz 1996. Size, density, and structure of comet Shoemaker-Levy-9 inferred from the physics of tidal breakup. *Icarus* **121**, 225–248.

Asphaug, E., W. Benz, S. J. Ostro, D. J. Scheere, E. M. DeJong, S. Suzuki, and R. S. Husdon 1996. Disruptive impacts into small asteroids. *BAAS* **28**, 1102.

Asphaug, E., and H. J. Melosh 1993. The Stickney impact of Phobos: A dynamic model. *Icarus* **101**, 144–164.

Belton, M. J. S., and 18 additional authors 1994a. Galileo encounter with 951 Gaspra: First pictures of an asteroid. *Science* **257**, 1647–1652.

Belton, M. J. S., and 19 additional authors 1994b. First images of asteroid 243 Ida. *Science* **265**, 785–788.

Belton, M. J. S., et al. 1995. Bulk density of asteroid 243-Ida from the orbit of its satellite Dactyl. *Nature* **374**, 785–788.

Belton, M. J. S., C. R. Chapman, K. P. Klaasen, A. P. Harch, P. C. Thomas, J. Veverka, A. S. McEwen, and R. J. Pappalardo 1996. Galileo's encounter with 243 Ida: An overview of the imaging experiment. *Icarus* **120**, 1–19.

Benner, L. A. M., *et al.* 1997. Radar Observations of Near-Earth Asteroid 2063 Bacchus. *Bull. Am. Astr. Soc.* **29**, 965.

Benz, W., and J. G. Hills 1987. Three-dimensional hydrodynamical simulations of stellar collisions I. Equal-mass main-sequence stars. *Astrophys. J.* **323**, 614–628.

Benz, W., J. G. Hills, and F.-K. Thielemann 1989. Three-dimensional hydrodynamical simulations of stellar collisions II. White dwarfs. *Astrophys. J.* **342**, 986–998.

Binney, J., and S. Tremaine 1987. *Galactic Dynamics*. Princeton Univ. Press, Princeton, NJ.

Boss, A. P. 1994. Tidal disruption of periodic comet Shoemaker-Levy-9 and a constraint on its mean density. *Icarus* **107**, 422–426.

Boss, A. P, A. G. W. Cameron, and W. Benz 1991. Tidal disruption of inviscid planetesimals. *Icarus* **92**, 165–178.

Bottke, W. F., and H. J. Melosh 1996a. The formation of asteroid satellites and doublet craters by planetary tidal forces. *Nature* **381**, 51–53.

Bottke, W. F., and H. J. Melosh 1996b. The formation of binary asteroids and doublet craters. *Icarus* **124**, 372–391.

Bottke, W. F., M. C. Nolan, and R. Greenberg 1994a. Velocity distributions among colliding asteroids. *Icarus* **107**, 255–268.

Bottke, W. F., M. C. Nolan, R. Greenberg, and R. A. Kolvoord 1994b. Collisional lifetimes and impact statistics of near-Earth asteroids. In *Hazards Due to Comets and Asteroids*, (T. Gehrels and M. S. Matthews, Eds.), pp. 337–357. University of Arizona, Tucson.

Bottke, W. F., D. C. Richardson, and S. G. Love 1997a. Can tidal disruption of asteroids make crater chains on the Earth and Moon?. *Icarus* **126**, 470–474.

Bottke, W. F., D. C. Richardson, and S. G. Love 1997b???. 1620 Geographos and 433 Eros: Resculpted by planetary tides???. *Nature???*, in press.

1)() '1 '11<1, W. F., D. C. Richardson, and S. G. I,()\rl 1998???. Production of Tunguska-sized bodies by the Earth's tidal forces. *Planet. Space Sci.*, in press.

Chapman, C. R. 1978. Asteroid collisions, craters, regolith, and lifetimes. In *Asteroids: An exploration assessment* (I). Morrison and W. C. Wells, Eds.). NASA Conf. Publ. 2053, pp. 225 242.

Chandrasekhar, S. 1969 *Ellipsoidal Figures of Equilibrium*. Yale Univ. Press, New Haven, CT

Chauvineau, B., I). Farinella, and A. W. Harris 1995. The evolution of Earth-approaching binary asteroids: a Monte-Carlo dynamical model. *Icarus* **115**, 36 46.

I).W' Is, D. R., and Chapman, C. R. 1977. Asteroid fragmentation processes and collisional evolution. *PGPI Meeting*, St. Louis.

Dobrovolskis, A. R. 1982. Internal stresses in Phobos and other triaxial bodies. *Icarus* **52**, 136 148.

Dobrovolskis, A. R. 1990. Tidal disruption of solid bodies. *Icarus* **88**, 24 38.

Farinella, P. 1992.. Evolution of Earth-crossing binary asteroids due to gravitational encounters with the Earth. *Icarus* **96**, 284 285.

Farinella, }'. and B. Chauvineau 1993. On the evolution of binary Earth-approaching asteroids. *Astron. Astrophys.* **279**, 251 259.

Goldstein, H. 1980. *Classical Mechanics*, 2nd ed. Addison-Wesley, Reading.

Greenberg, R., M. C. Nolan, W. 1". Bottke, R. A. Kolvoord, and J. Veverka 1994. Collisional history of Gaspra. *Icarus* **107**, 84-97.

Greenberg, R., W. F. Bottke, M. C. Nolan, P. Geissler, J. M. Petit, D. D. Durda, E. Asphaug, and J. Head 1996. Collisional and dynamical history of Ida. *Icarus* **120**, 106 I IN.

Harris, A. W. 1996. The rotation rates of vellyasteroids: Evidence for "rubble-pile" structure. //////(1/' /'/(///(/. *Sci.* **XXVII**, 193 194.

11(11)SON, R. S., and S. J. Ostro 1995a. Shape of asteroid 1769 Castalia (1989 PB) from inversion of radar images. *Science* 263, 940 943.

Hudson, R. S., and S. J. Ostro 1995b. Shape and nonprincipal axis spin-state of asteroid 4179 Toutatis. *Sc* /(//((270, 84 86.

Jeffreys, H. 1947. The relation of cohesion to Roche's limit. *Mon. Not. R. Astron. Soc.* **107**, 260 272.

Kaula, W. M., and A. E. IM,,\('iII;}' 1984. Mechanical models of close appraches and collisions of large protoplanets. In *Origin of the Moon* (\ I'. Ii. Hartmann, R J. Phillips, and G. J. Taylor, Eds.). Lunar and Planetary Institute, Houston.

Love, S. G., and Ahrens, '1 J. 1996. Catastrophic impacts on gravity dominated asteroids. *Icarus*, in press.

Love, S. G., 1). E. Brownlee, N. L. King, and i'. Hörz 1995. Morphology of meteoroid and debris impact craters formed in soft metal targets on the LDEF satellite. *International J. Impact Engineering* **16**, 405 418.

McFadden, L. A., I). J. Tholen, and G. J. Veeder 1989. Physical properties of Aten, Apollo, and Amor asteroids. In *Asteroids II*, (R. I). Binzel, '1'. Gehrels, and M. S. Matthews, Eds.), pp. 442 467. University of Arizona, Tucson.

Melosh, 11. J. 1989 *Impact Cratering: A Geologic Process*. Oxford University Press, New York.

Melosh, H. J., and P. Schenk 1993. Split comets and the origin of crater chains on Ganymede and Callisto. *Nature* **365**, 731 733.

Melosh, H. .1. , and J. A. Stansberry 1991.. Double craters and the tidal disruption of binary asteroids. *Icarus* **94**, 171 179.

Melosh, H. J., and E. A. Whitaker 1994. Lunar crater chains. *Nature* **365**, 713.

Menichella, M., P. Paolicchi, and P. Farinella 1996. The main-belt as a source of near-Earth asteroids. *Earth, Moon, and Planets* **72**, 133–149.

Michel, P., Ch. Froeschlé, and P. Farinella 1996. Dynamical evolution of NEAs: Close encounters, secular perturbations and resonances. *Earth, Moon, and Planets* **72**, 151–164.

Mizuno, H., and A. P. Boss 1985. Tidal disruption of dissipative planetesimals. *Icarus* **63**, 109–133.

Morbidelli, A., and M. Moons 1995. Numerical evidence on the chaotic nature of the 3/1 mean motion commensurability. *Icarus* **115**, 60–65.

Morrison, D., Ed. 1992 *The Spaceguard Survey. Report of the NASA international near-earth-object detection workshop.* NASA, Washington, D.C.

Ocampo, S. C., and K. O. Pope 1996. Shuttle imaging radar SIR-C: Images reveal multiple craters at Aorounga, northern Chad. *Lunar Planet. Sci.* **27**, 977–978.

Öpik, E. J. 1950. Roche's limit: Rings of Saturn. *Irish Astr. J.* **1**, 25–26

Öpik, E. J. 1966. Sun-grazing comets and tidal disruption. *Irish Astr. J.* 7, 141-161

Ostro, S. J. 1993. Planetary radar astronomy. *Rev. Mod. Phys.* **65**, 1235–1279

Ostro, S. J., et al. 1995a. Extreme elongation of asteroid 1620-Geographos from radar images. *Nature* **375**, 474–477.

Ostro, S. J., et al. 1995b. Radar images of asteroid-4179 Toutatis. *Science* **270**, 80–83.

Ostro, S. J., et al. 1996. Radar observations of asteroid 1620-Geographos. *Icarus* **121**, 46–66.

Petit, J.-M., and M. Hénon 1987. A numerical simulation of planetary rings. I. Binary encounters. *Astron. Astrophys.* **173**, 389–404.

Press, W. H. and D. N. Spergel 1988. Choice of order and extrapolation method in Aarseth-type N-body algorithms. *Astrophys. J.* **325**, 715–721.

Press, W. H., S. A. Teukolsky, W. T. Vetterling, and B. P. Flannery 1992. *Numerical Recipes in C: The Art of Scientific Computing*, 2nd ed. Cambridge Univ. Press, Cambridge.

Rabinowitz, D. L. 1994. The size and shape of the near-earth asteroid belt. *Icarus* **111**, 364–377

Rabinowitz, D. L., et al. 1993. Evidence for a near-earth asteroid belt. *Nature* **363**, 704–706

Rampino, M. R., and T. Volk 1996. Multiple impact event in the Paleozoic: Collision with a strong of comets or asteroids?. *Geophys. Res. Lett.* **23**, 49–52.

Richardson, D. C. 1993. A new tree code method for simulations of planetesimal dynamics. *Mon. Not. R. Astron. Soc.* **261**, 396–414.

Richardson, D. C. 1994. Tree code simulations of planetary rings. *Mon. Not. R. Astron. Soc.* **269**, 193–511.

Richardson, D. C. 1995. A self-consistent numerical treatment of fractal aggregate dynamics. *Icarus* **115**, 320–335.

Richardson, D. C., E. Asphaug, and L. Benner 1995. Comet Shoemaker-Levy 9: A 'Rubble Pile' Model with Dissipative Collisions and Gravitational Perturbations. AAS Division for Planetary Sciences, 27th Annual Meeting.

Rickman, H. 1979. Recent dynamical history of the six short-period comets discovered in 1975. In *Dynamics of the Solar System* (R. L. Duncombe, Ed.), pp. 293–298. D. Reidel, Dordrecht.

Rickman, H., and A. M. Malmort 1981. Variations of the orbit of comet P/Gehrels 3: Temporary satellite captures by Jupiter. *Astron. Astrophys.* **102**, 165–170.

Schenk, P. M., E. Asphaug, W. B. McKinnon, H. J. Melosh, and P. R. Weissman 1996. Cometary nuclei and tidal disruption: the geologic record of crater chains on Callisto and Ganymede. *Icarus* **121**, 249–274.

Schultz, P. H., and D. I Gault 1985. Clustered impacts: Experiments and implications. *J. Geophys. Res.* **90**, 3701–3732.

Sekiguchi, N. 1970. On the fission of a solid body under influence of tidal force. *Moon* **1**, 429–439.

Sekanina, Z., and I K Yeomans 1985. Orbital motion, nucleus precession, and splitting of periodic comet Brooks 2. *Astron. J.* **90**, 2335–2352.

Solem, J. C., and J. G. Hills 1996. Shaping of Earth-crossing asteroids by tidal forces. *Astron. J.* **111** 1382–1387.

Sridhar, S. and S. Tremaine 1992. Tidal disruption of viscous bodies. *Icarus* **95**, 86–99.

Thomas, P., M. J. S. Belton, B. Carcich, C. R. Chapman, M I Davies, R. Sullivan, and J. Veverka 1996. The shape of Ida. *Icarus* **120**, 20–32.

Thomas, P., J. Veverka, J. Bell, J. Lunine, and D. Cruikshank 1992. Satellites of Mars: Geologic History. In *Mars*, (H. H Kieffer, B. M. Jakosky, C. W. Snyder, and M. S. Matthews, Eds.), pp. 1257–1282. University of Arizona, Tucson.

Wasson, J. T. 1974. *Meteorites*. Springer-Verlag, New York.

Weissman, P. R. 1980. Physical loss of long-period comets. *Astron. Astrophys.* **85**, 91–106.

Weissman, P. R. 1982. Terrestrial impact rates for long- and short-period comets. *GSA Special Pap.* **190**, 15–24.

Wisdom, J. 1983. Chaotic behavior and the origin of the 3/1 resonance. *Icarus* **56**, 51–74.

Witchman, R. W., and C. A. Wood 1995. The Davy crater chain: Implications for tidal disruption in the Earth-Moon system and elsewhere. *Geophys. Res. Lett.* **22**, 583–586.

Yeomans, W. 1997. TITLE???. *Science* in press.

Table 1: Results for the $P = 6\text{h}$ elongated progenitor encountering the Earth.

q	v_∞	θ	C	δR	$P_{\rm rem}$	$\varepsilon_{\rm rem}$	$M_{\rm rem}$	$M_{\rm acc}$	$M_{\rm orb}$	$M_{\rm esc}$	Notes
1.0	3	44	S	0.18	-7.5	0.15	0.105		0.008	0.887	
1.0	6	50	S	0.34	4.5	0.45	0.146			0.854	
1.0	9	41	S	0.25	7.1	0.28	0.146		0.004	0.851	
1.0	12	64	S	0.40	7.5	0.18	0.312	0.081	0.008	0.599	
1.0	15	26	S	0.28	7.6	0.13	0.287	0.004	0.004	0.704	
1.0	18	50	S	0.41	6.4	0.19	0.377		0.437	0.186	
1.0	21	54	B	0.51	4.9	0.43	0.785	0.158	0.008	0.049	
1.0	24	41	B	0.56	6.7	0.58	0.785	0.154	0.019	0.012	
1.4	3	64	S	0.47	4.6	0.55	0.267		0.008	0.725	
1.4	6	37	S	0.35	4.7	0.18	0.251		0.012	0.737	Fig. 2a
1.4	9	38	S	0.35	5.7	0.22	0.348		0.077	0.575	
1.4	12	69	B	0.80	5.1	0.44	0.850		0.024	0.125	†
1.4	15	37	B	0.73	5.0	0.64	0.883	0.105	0.008	0.004	
1.4	18	51	M	1.06	5.3	0.65	0.968		0.024	0.008	
1.4	21	54	M		4.5	0.62	0.988			0.012	
1.4	24	41	M		4.8	0.59	0.996			0.004	
1.8	3	60	S	0.47	4.8	0.25	0.437		0.263	0.300	
1.8	6	55	B	0.80	5.0	0.55	0.725		0.032	0.243	
1.8	9	34	B	0.34	5.1	0.32	0.696		0.275	0.028	
1.8	12	59	M	0.95	5.5	0.57	0.935		0.032	0.032	
1.8	15	21	N		4.4	0.51	1				†
1.8	18	51	N		4.3	0.52	1				
1.8	21	53	N		4.3	0.49	1				
1.8	24	40	N		4.6	0.54	1				
2.2	3	26	S	0.37	4.3	0.23	0.494		0.004	0.502	
2.2	6	26	B	0.65	4.4	0.44	0.870		0.117	0.012	Fig. 2b
2.2	9	32	M	0.77	4.8	0.54	0.939		0.016	0.045	Fig. 2c
2.2	12	62	N		3.9	0.50	1				
2.2	15	35	N		4.1	0.47	1				
2.2	18	52	N		4.1	0.44	1				
2.2	21	57	N		4.2	0.41	1				
2.2	24	41	N		4.5	0.44	1				

Table I, continued.

q	v_∞	θ	C	δR	$P_{\rm rem}$	$\varepsilon_{\rm rem}$	$M_{\rm rem}$	$M_{\rm acc}$	$M_{\rm orb}$	$M_{\rm esc}$	Notes
2.6	3	37	B	0.33	4.5	0.24	0.798			0.202	
2.6	6	44	M	0.84	4.3	0.54	0.955		0.024	0.020	
2.6	9	31	M		4.0	0.54	0.996		0.004		
2.6	12	63	N		4.0	0.42	1				
2.6	15	35	N		4.2	0.43	1				
2.6	18	53	N		4.4	0.44	1				
2.6	21	56	N		4.6	0.42	1				
2.6	24	42	N		4.7	0.43	1				
3.0	3	45	M	02	4.0	0.51	0.964		0.012	0.024	
3.0	6	21	N		3.8	0.43	1				†
3.0	9	31	N		3.9	0.43	1				Fig 2d
3.0	12	66	N		4.3	0.42	1				†
3.0	15	34	N		4.5	0.43	1				
3.0	18	53	N		4.6	0.43	1				
3.0	21	57	N		4.9	0.42	1				
3.0	24	40	N		4.9	0.43	1				
3.4	3	68	N		3.8	0.44	1				†
3.4	6	40	N		3.8	0.44	1				
3.4	9	23	N		4.3	0.42	1				†
3.4	12	55	N		4.4	0.43	1				
3.4	15	54	N		4.6	0.43	1				
3.4	18	53	N		4.8	0.43	1				
3.4	21	57	N		4.9	0.43	1				
3.4	24	42	N		5.0	0.43	1				
3.8	3	66	N		4.0	0.41	1				†
3.8	6	20	N		4.3	0.41	1				†
3.8	9	29	N		4.4	0.43	1				
3.8	12	51	N		4.5	0.43	1				
3.8	15	35	N		4.8	0.43	1				
3.8	18	53	N		4.9	0.42	1				
3.8	21	58	N		5.1	0.42	1				
3.8	24	41	N		5.1	0.42	1				

Figure Captions

Figure 1: Diagram illustrating the two spin axis orientation angles α and β, and the periapse body orientation angle θ (note how θ is measured in the orbital plane). The example shown has an unfavorable orientation for breakup, i.e., $\theta > 90°$.

Figure 2: ***OUT OF DATE, may be replaced by evolution plots*** Snapshots of four classes of tidal disruption. In decreasing order of severity: (a) S class "Shoemaker-Levy-9-type" catastrophic disruption where the progenitor forms into a line of roughly equal size clumps (i.e., a "string of pearls") and leaves less than 50% of its mass in the largest fragment; (b) B class breakup with mass shedding of clumps and single particles, leaving the progenitor with 50%–90% of its original mass; (c) M class mild mass shedding of clumps or particles, leaving the progenitor with over 90% of its original mass; and (d) N class with no mass loss but possible reshaping of the progenitor accompanied by spin-up or spin-down.

Figure 3: Train lengths as a function of normalized time for the 11 S class outcomes of the $P = 6$h case from Fig. 4. Time $t = 1$ corresponds to the end of each simulation while $t = 0$ is close to the time of perigee passage. The train length at $t = 0$ is equal to the original progenitor size, about 2 km. Note that due to differences in the encounter speed v_∞, the termination distances for these runs were reached at different times, which is why the abscissa has been normalized for easy comparison. The case shown in Fig. 2a is indicated with a dashed line here. Note that in all case the train lengths grow almost linearly, consistent with a hyperbolic flyby.

Figure 4: Tidal disruption outcomes for elongated rubble-pile progenitors with a variety of rotation periods encountering the Earth for various values of q and v_∞. The plots have been scaled for easier comparison of the range of parameter space explored for each P value. The $P = \infty$ case corresponds to zero spin.

Figure 5: Outcome plot for $P = 6$ h encounters with the Moon. Compare with $P = 6$ h in Fig. 4 Disruption of ECAs is much more difficult in the vicinity of the Moon.

Figure 6: A graphic illustration of the final configurations of each of the $P = 6$ h Earth encounters. Compare with Fig. 4. Each image has been scaled to fit exactly inside its box, so the N class outcomes are zoomed views of the progenitor whereas S class outcomes are seen from distances as much as 500 km away.

Figure 7: This set of plots show the effect of varying α and β for two sets of $P = 6$ h and $v_\infty = 6$ km s^{-1} Earth encounters, one with $q = 1.4\ R_\oplus$, the other $q = 2.2\ R_\oplus$. For each case, the uppermost plot shows the effect of varying α while restricting the rotation axis to the xz-plane ($\beta = 0°/180°$) while the other plot corresponds to $\beta = \pm 90°$ (the yz-plane). For the $q = 1.4\ R_\oplus$ case, the zero-tilt outcome is S class. As the rotation angle approaches 90°, the mass loss drops steeply until for $\alpha > 90°$ the outcome becomes N class. Note that this transition is not quite as steep for $\beta = \pm 90°$ because the long axis of the asteroid continues to sweep towards and away from the planet so the elongation can still assist the breakup.

Figure 8: Outcome plot for a retrograde $P = 12$ h case. Compare with $P = 12$ h and $P = \infty$ in Fig. 4. Retrograde rotation causes resistance to tidal breakup so the range of q and v_∞ for which mass loss occurs is reduced. It is still possible to get S class outcomes however, for small enough q and v_∞. As the retrograde spin increases, though, the mass loss region shrinks even further.

Figure 9: Outcome plot for a near-spherical $P = 6$ h (prograde) encounter with the Earth. Compare with $P = 6$ h in Fig. 4. Note how the lack of a significant moment arm drastically reduces the disruption region.

Figure 1

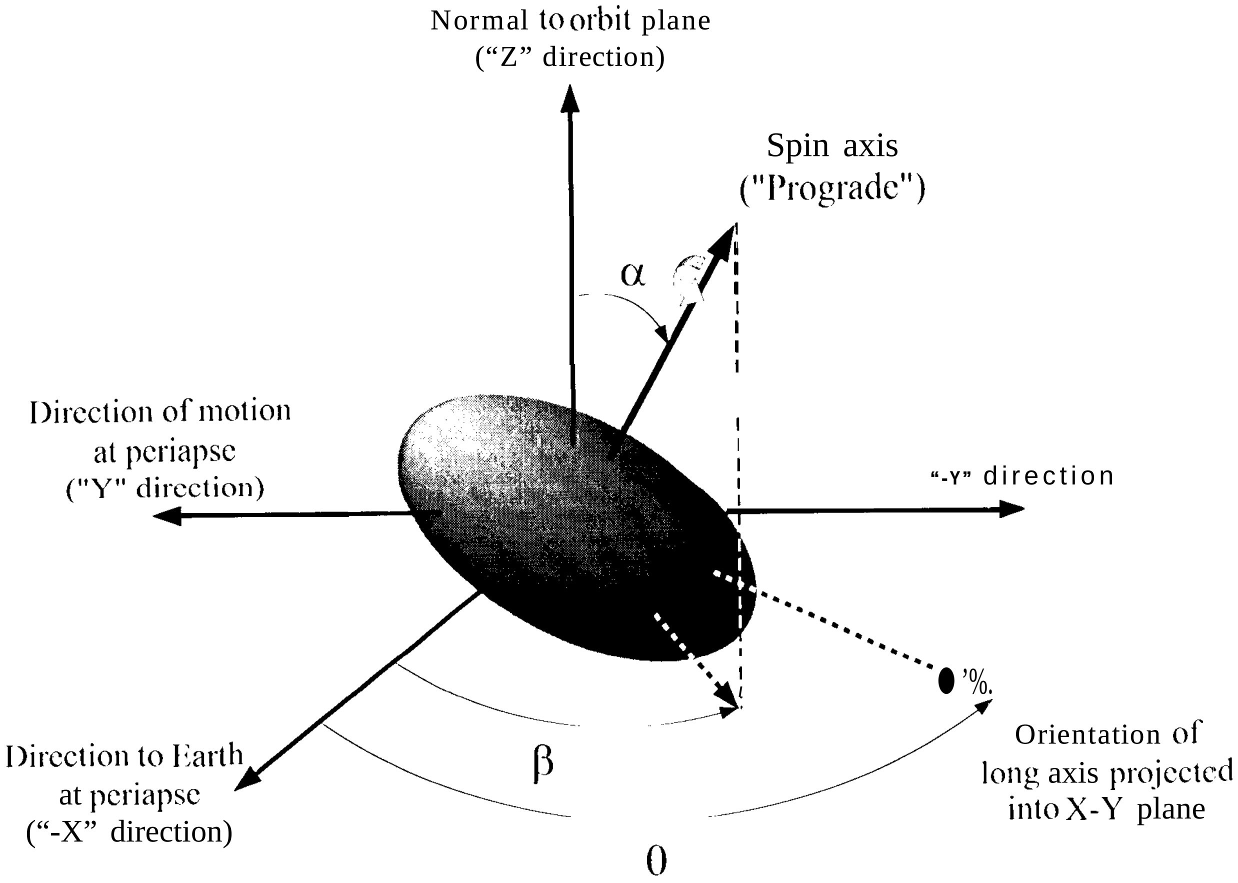
Normal to orbit plane
("Z" direction)
Spin axis
("Prograde")
α
Direction of motion
at periapse
("Y" direction)
"-Y" direction
'%.
Orientation of
long axis projected
into X-Y plane
Direction to Earth
at periapse
("-X" direction)
β
0

Figure 2

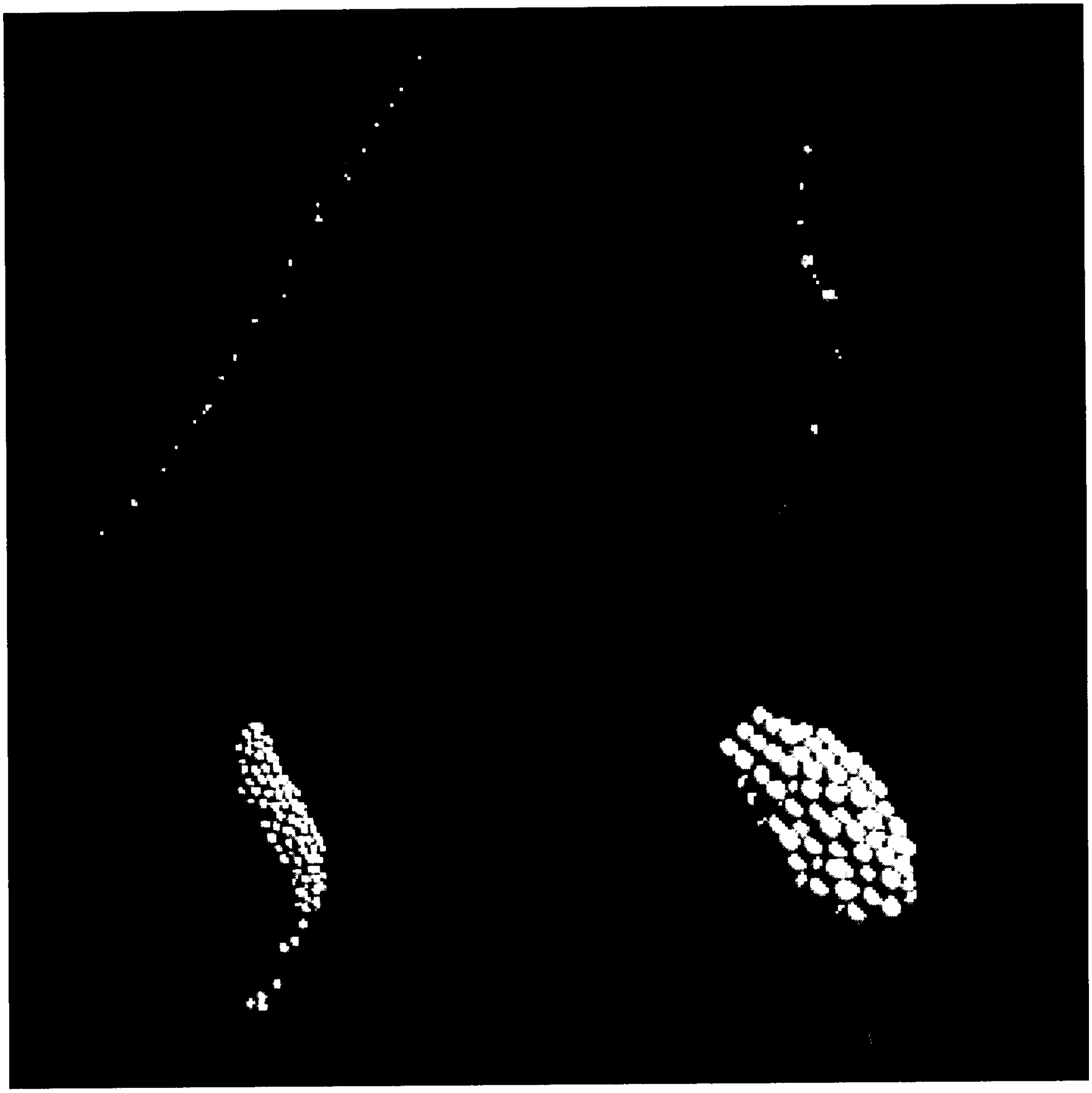

Figure 3

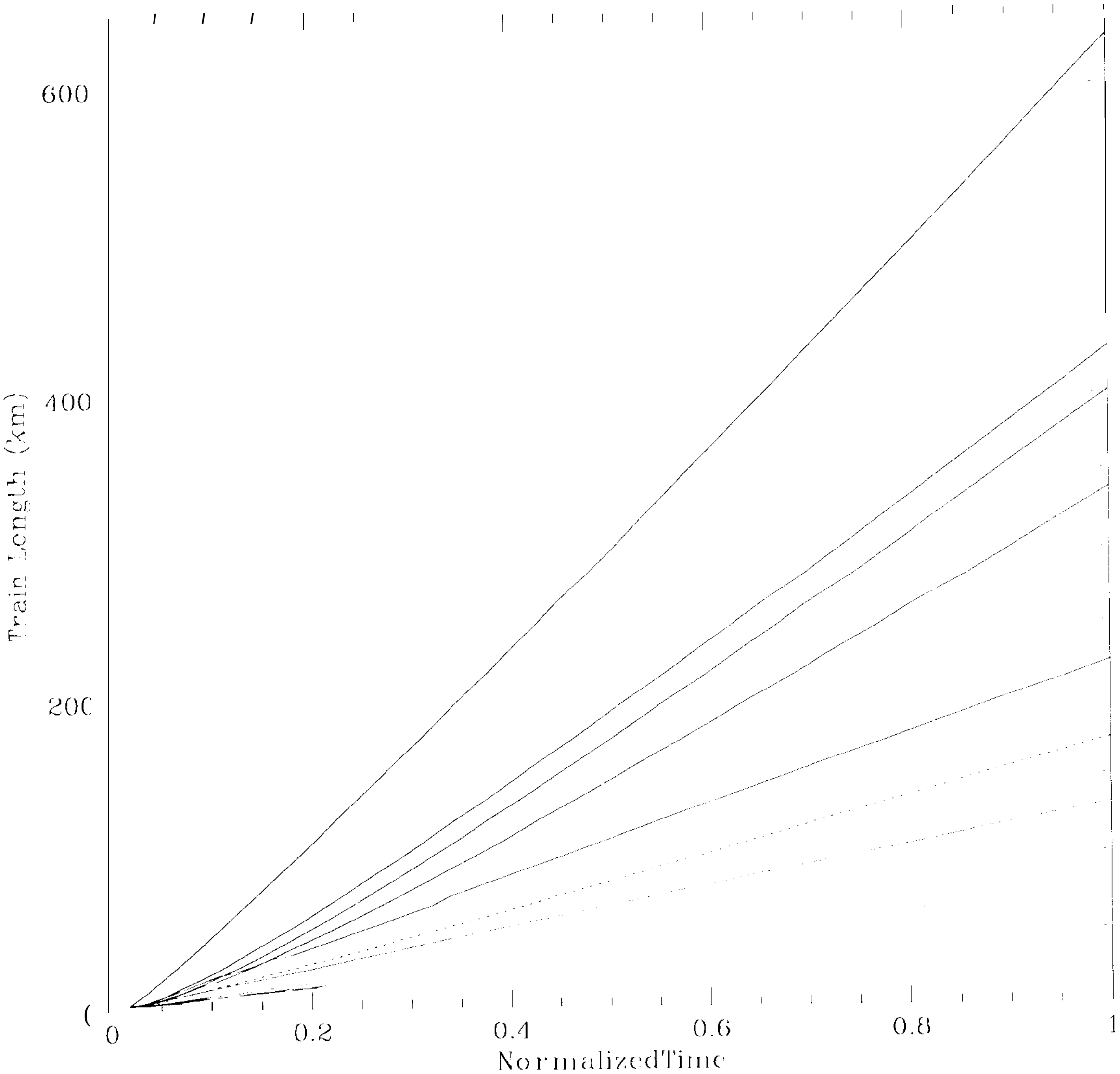

Figure 4

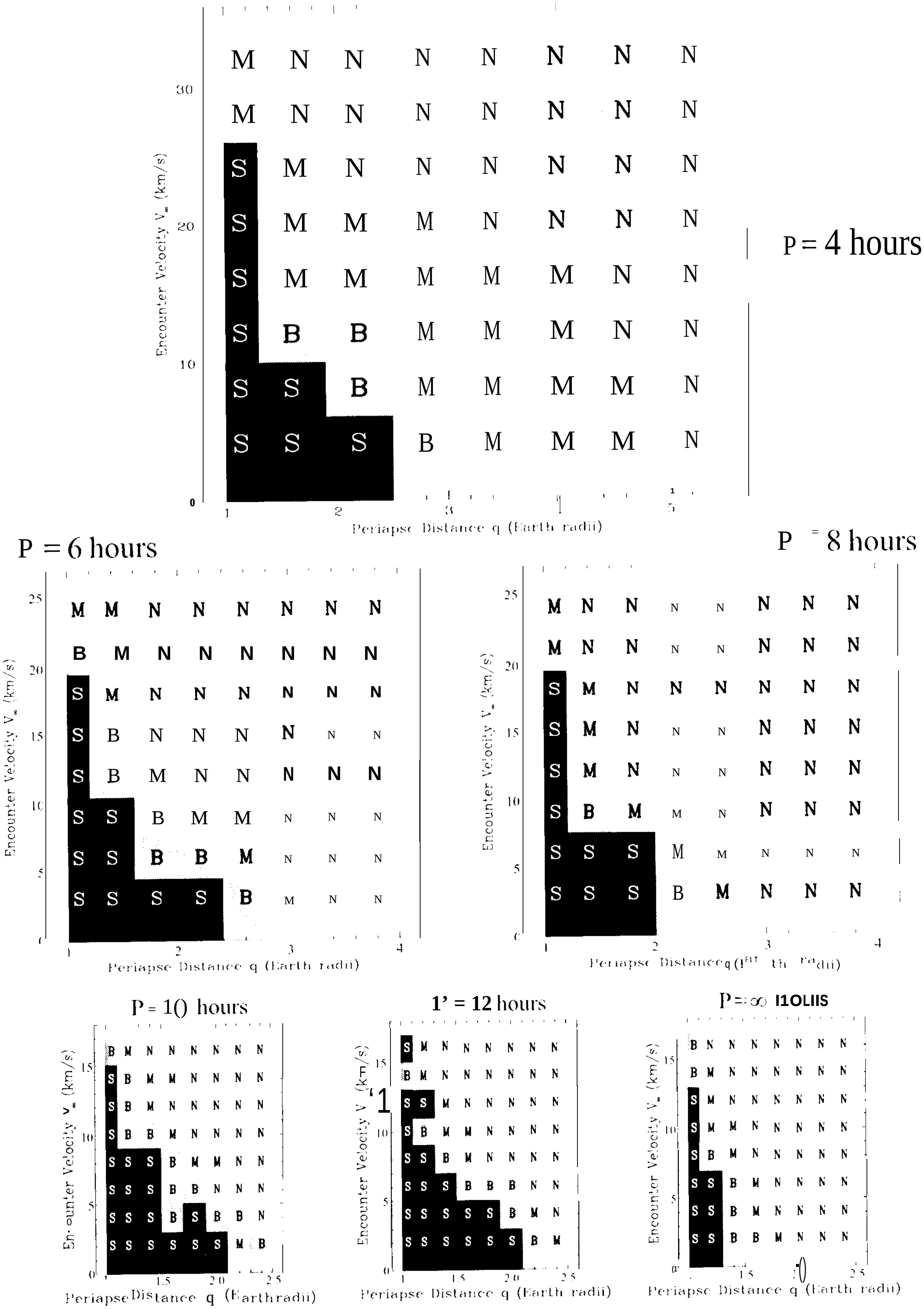
P = 4 hours
Encounter Velocity V_∞ (km/s)
30
20
10
0
M N N N N N N N
M N N N N N N N
S M N N N N N N
S M M M N N N N
S M M M M M N N
S B B M M M N N
S S B M M M M N
S S S B M M M N
1
2
3
5
Periapse Distance q (Earth radii)
P = 6 hours
Encounter Velocity V_∞ (km/s)
25
20
15
10
5
0
M M N N N N N N
B M N N N N N N
S M N N N N N N
S B N N N N N N
S B M N N N N N
S S B M M N N N
S S B B M N N N
S S S S B M N N
1
2
3
4
Periapse Distance q (Earth radii)
P = 8 hours
Encounter Velocity V_∞ (km/s)
25
20
15
10
5
0
M N N N N N N N
M N N N N N N N
S M N N N N N N
S M N N N N N N
S M N N N N N N
S B M M N N N N
S S S M M N N N
S S S B M N N N
1
2
3
4
Periapse Distance q (Earth radii)
P = 10 hours
Encounter Velocity V_∞ (km/s)
15
10
5
0
B M N N N N N N
S B M M N N N N
S B M N N N N N
S B B M N N N N
S S S B M M N N
S S S B B N N N
S S S B S B B N
S S S S S S M B
1.5
2.0
2.5
Periapse Distance q (Earth radii)
P = 12 hours
Encounter Velocity V_∞ (km/s)
15
10
5
0
S M N N N N N N
B M N N N N N N
S S M N N N N N
S B M M N N N N
S S B M N N N N
S S S B B B N N
S S S S S B M N
S S S S S S B M
1
1.5
2.0
2.5
Periapse Distance q (Earth radii)
P = ∞ hours
Encounter Velocity V_∞ (km/s)
15
10
5
0
B N N N N N N N
B M N N N N N N
S M N N N N N N
S M M N N N N N
S B M N N N N N
S S B M N N N N
S S B M N N N N
S S B B M N N N
1.5
2.0
2.5
Periapse Distance q (Earth radii)

Figure 5

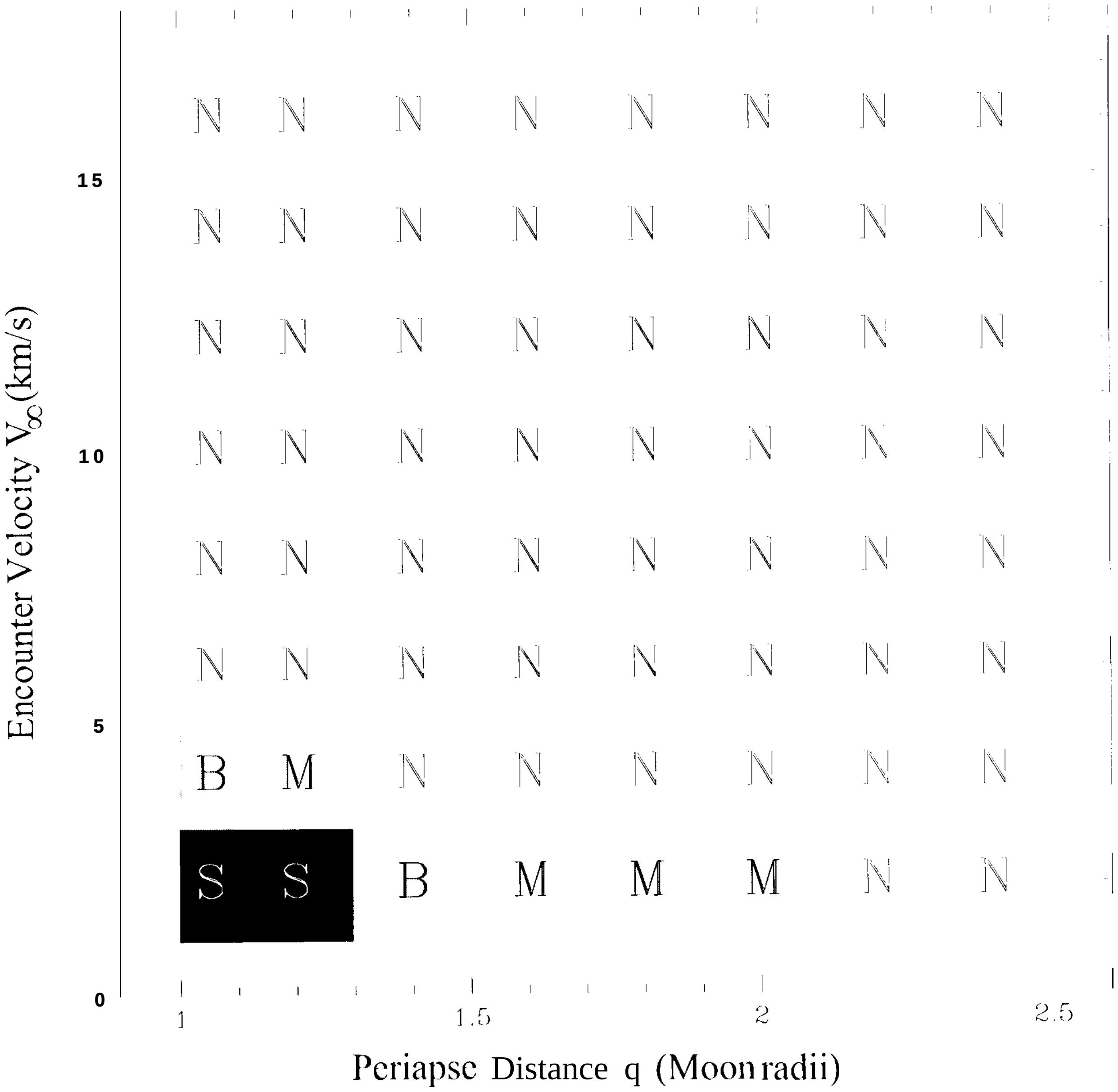
Encounter Velocity V_∞ (km/s)
0
5
10
15
1
1.5
2
2.5
Periapse Distance q (Moon radii)
N N N N N N N N
N N N N N N N N
N N N N N N N N
N N N N N N N N
N N N N N N N N
N N N N N N N N
B M N N N N N N
S S B M M M N N

Figure 6

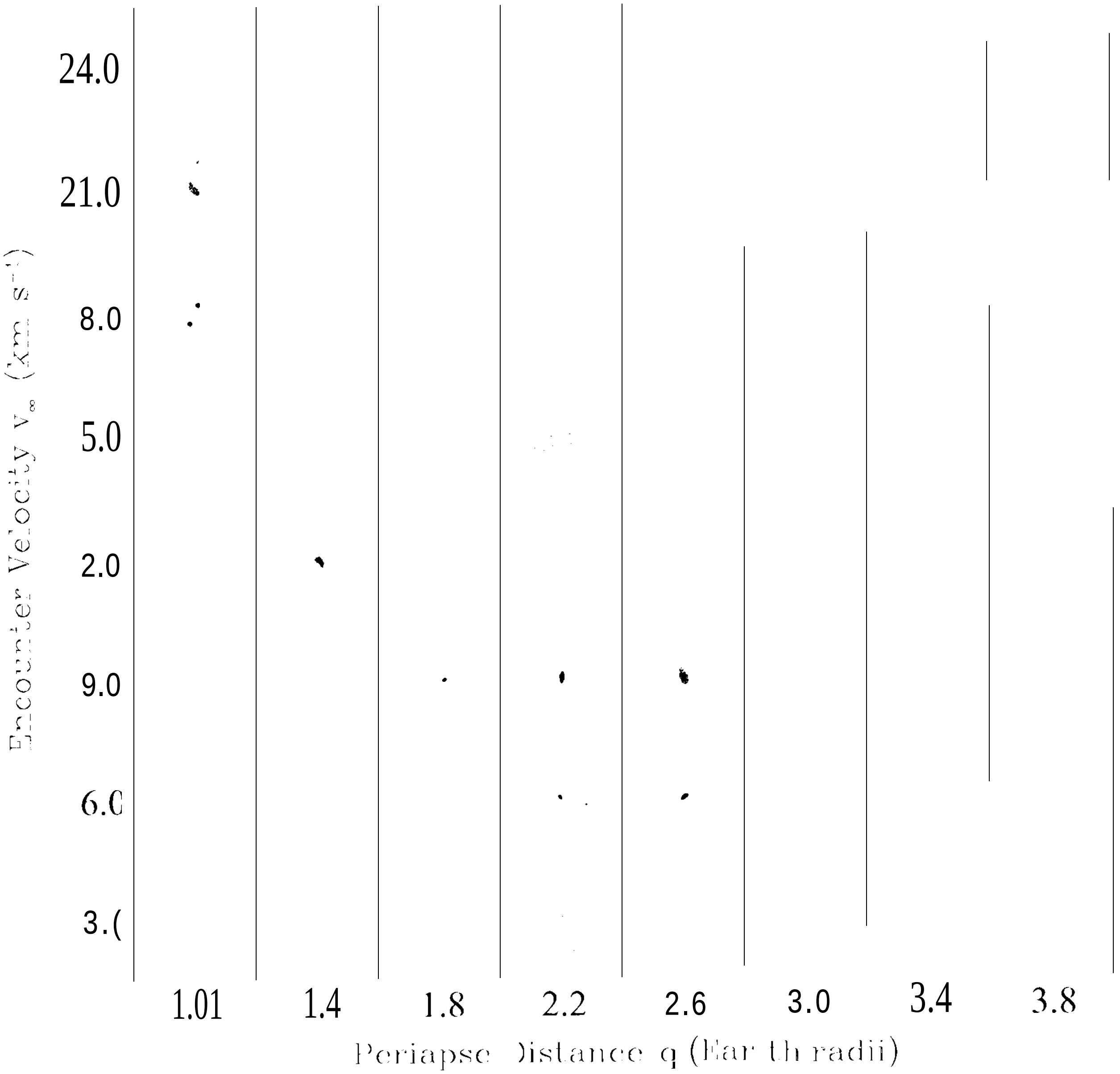
24.0
21.0
8.0
5.0
2.0
9.0
6.0
3.0
Encounter Velocity v∞ (km s⁻¹)
1.01
1.4
1.8
2.2
2.6
3.0
3.4
3.8
Periapse Distance q (Earth radii)

Figure 7

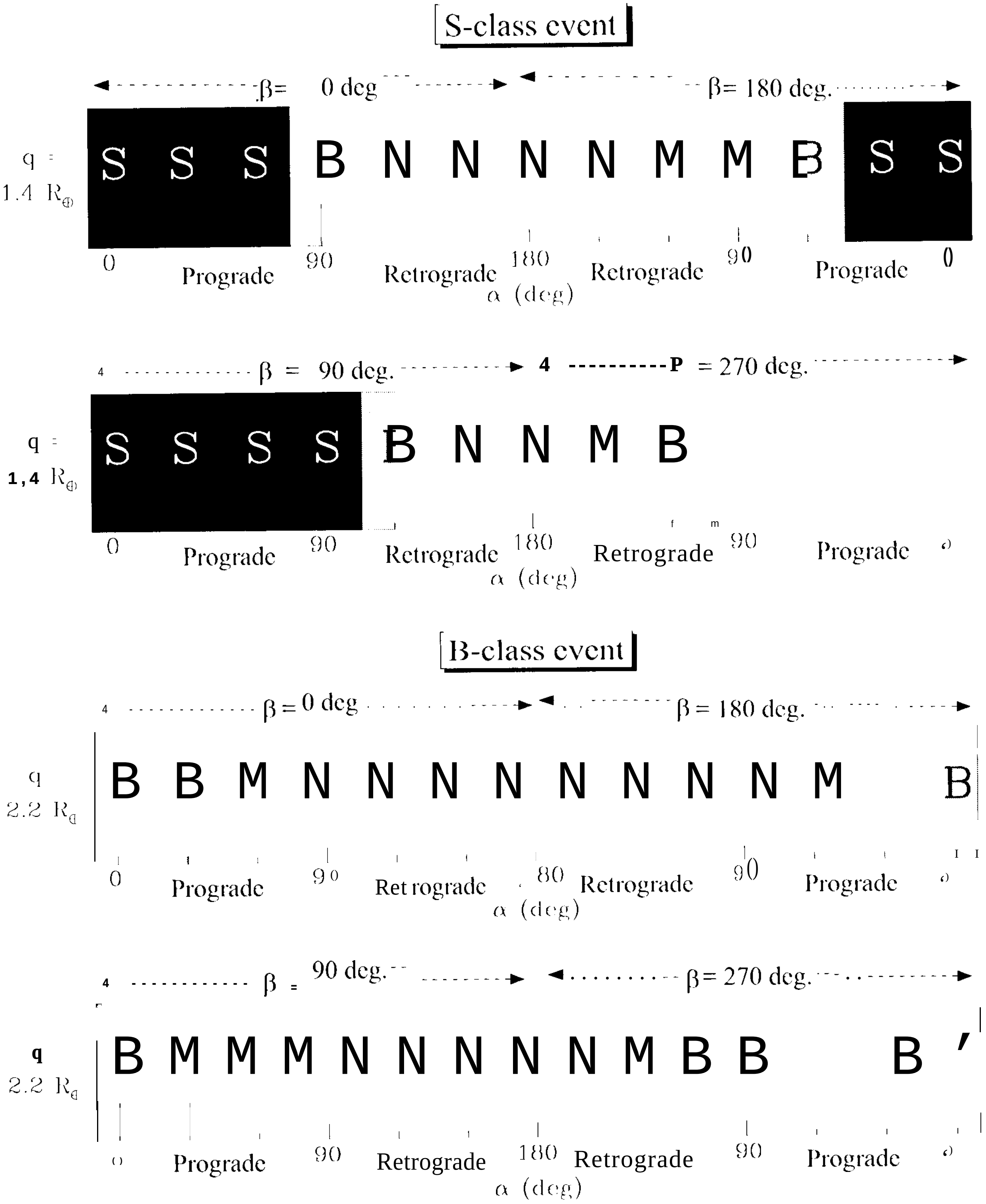
S-class event
β= 0 deg
β= 180 deg.
q = 1.4 R⊕
S S S B N N N N M M B S S
0 Prograde 90 Retrograde 180 Retrograde 90 Prograde 0
α (deg)
β = 90 deg.
β = 270 deg.
q = 1,4 R⊕
S S S S B N N M B
0 Prograde 90 Retrograde 180 Retrograde 90 Prograde 0
α (deg)
B-class event
β = 0 deg
β = 180 deg.
q = 2.2 R⊕
B B M N N N N N N N N M B
0 Prograde 90 Retrograde 180 Retrograde 90 Prograde 0
α (deg)
β = 90 deg.
β = 270 deg.
q = 2.2 R⊕
B M M M N N N N N M B B B
0 Prograde 90 Retrograde 180 Retrograde 90 Prograde 0
α (deg)

Figure 8

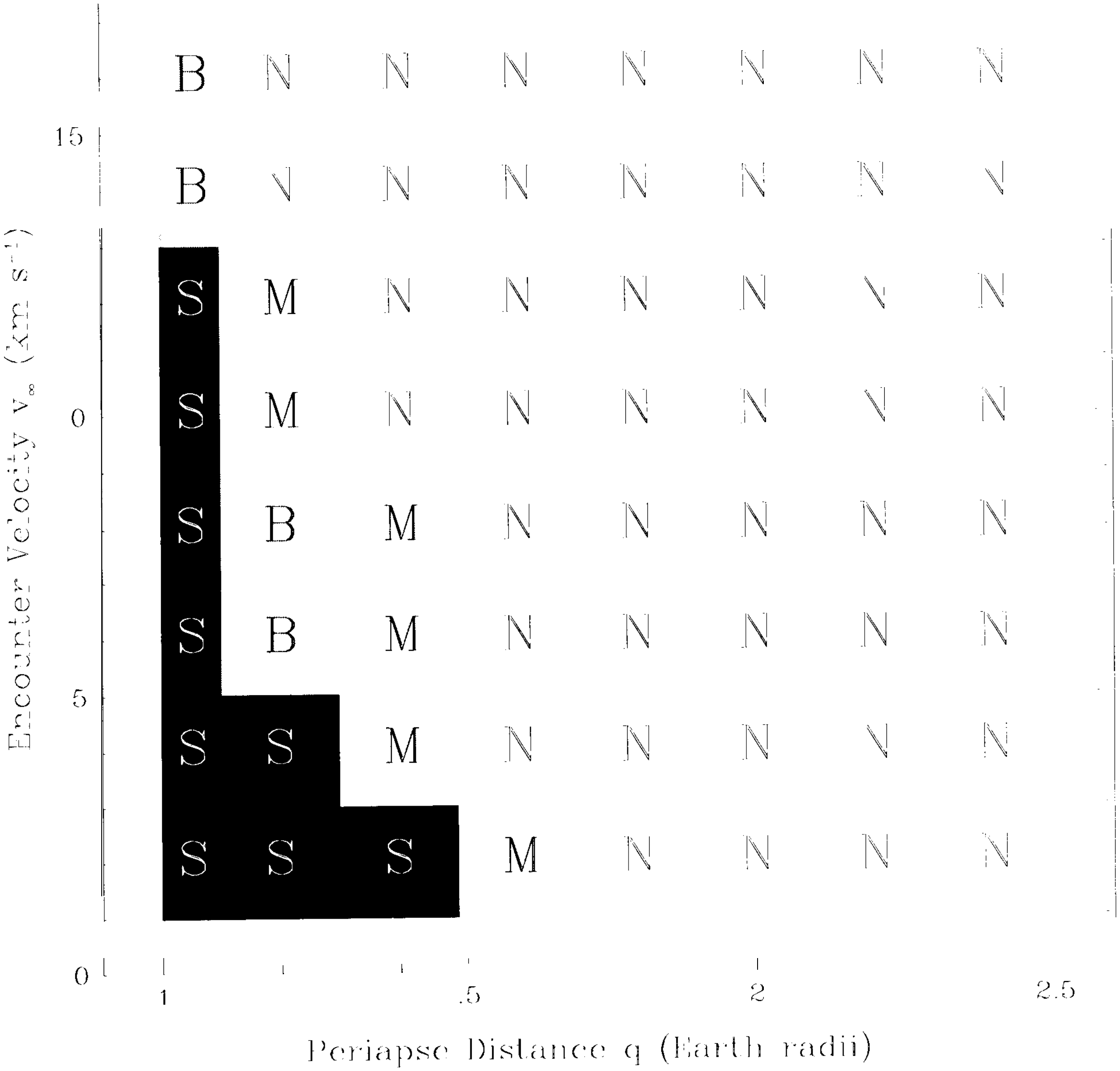

Encounter Velocity v_∞ (km s^{-1})
15
0
5
0
Periapse Distance q (Earth radii)
1
.5
2
2.5
B N N N N N N N
B N N N N N N N
S M N N N N N N
S M N N N N N N
S B M N N N N N
S B M N N N N N
S S M N N N N N
S S S M N N N N

Figure 9

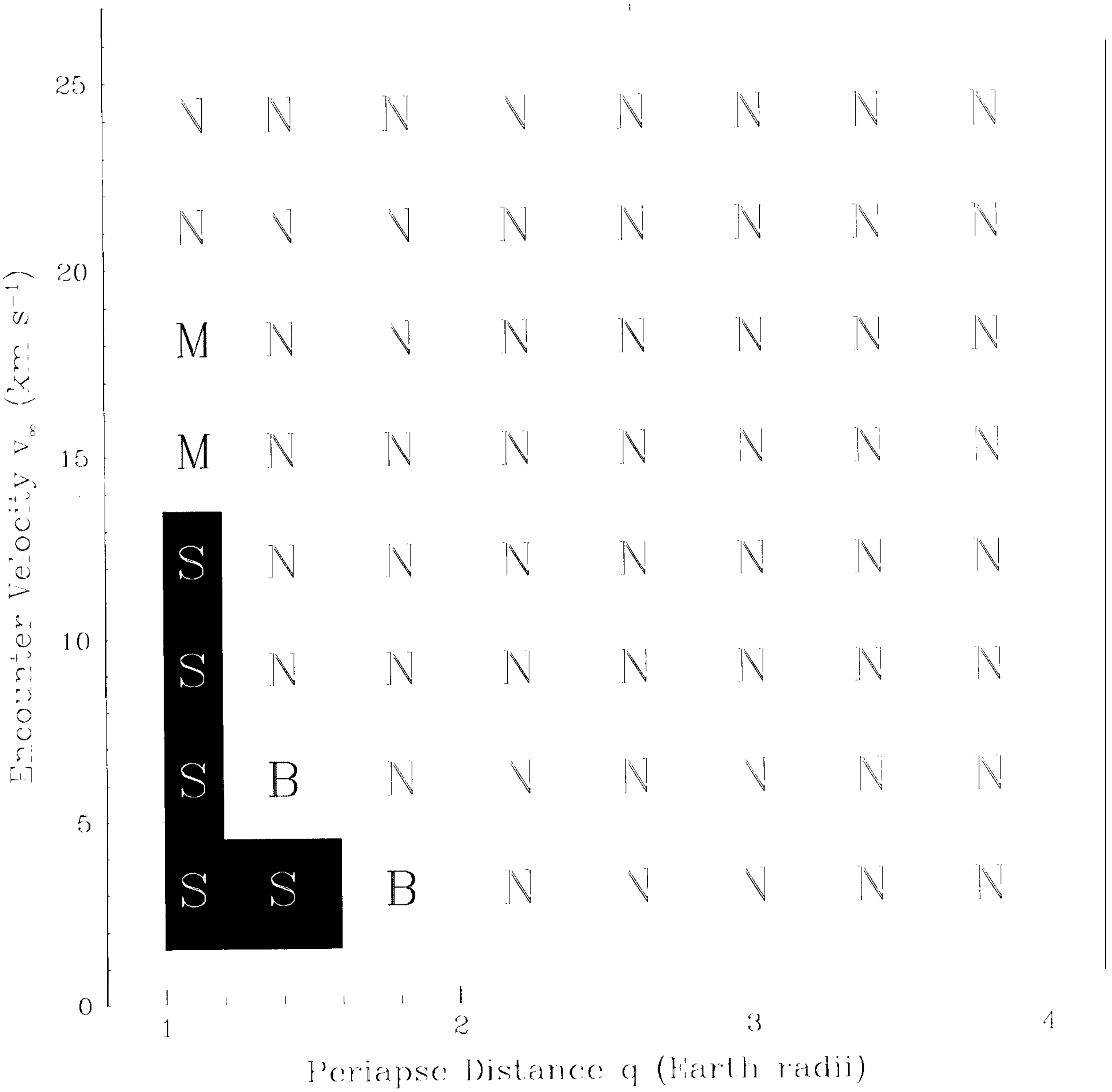
Encounter Velocity v_∞ (km s^{-1})
0
5
10
15
20
25
Periapse Distance q (Earth radii)
1
2
3
4
N N N N N N N N
N N N N N N N N
M N N N N N N N
M N N N N N N N
S N N N N N N N
S N N N N N N N
S B N N N N N N
S S B N N N N N